Light Water Reactor Sustainability Program

Modeling Strategy to Assess Radiation Induced Segregation and Phase Stability in Austenitic Steels in Light Water Reactors During Extended service: Milestone 7 Report

September 30, 2015

U.S. Department of Energy
Office of Nuclear Energy

Modeling Strategy to Assess Radiation Induced Segregation and Phase Stability in Austenitic Steels in Light Water Reactors During Extended service: Milestone 7 Report

Mahmood Mamivand (University of Wisconsin, Madison)
Ying Yang (Oak Ridge National Laboratory, Oak Ridge)
Dane Morgan (University of Wisconsin, Madison)

September 30, 2015

Prepared for the
U.S. Department of Energy
Office of Nuclear Energy

CONTENTS

FIGURES

SUMMARY

This report has been assembled to address the seventh milestone of the project entitled "Modeling Strategy to Assess Radiation Induced Segregation and Phase Stability in Austenitic Steels in Light Water Reactors during Extended Service," (also listed under "Irradiation-Induced Phase Transformations in High-Fluence Core Internals") which was defined as follows:

September 30, 2015: M3LW-15OR0402053 - complete report on the application of cluster dynamics model to establish radiation enhanced diffusion parameters.

The document summarizes our deliverables for the above milestone. It further discusses the application of this model to precipitation modeling, which was the motivation for building the model. Specifically, we discuss radiation enhanced diffusion and precipitation of carbides and γ' in cold-worked 316 stainless steels (SS). Section 1 describes the governing equations of the defect evolution cluster dynamics (CD) model and its parameterization for 316 SS. The CD model is fitted to experimental loop size and number density and then it is used to predict the evolution of single vacancies and total dislocations. Section 2 covers the modeling of precipitation of second phases in cold-worked 316 SS. First the equilibrium thermodynamics of available phases under LWR conditions is discussed. Then the predicted single vacancy and total dislocation values from section 1 are used to study the evolution of carbides and γ' in cold-worked 316 SS. The CD-informed thermo-kinetic model successfully captures the evolution of γ' volume fraction in cold-worked 316 SS under irradiation. For carbides the modeling results are not consistent with experimental data. We propose that radiation enhanced dissolution or carbon depletion at sinks could be the main sources of this inconsistency and are topics that should be addressed in future work. We build the model for fast reactor conditions due to the availability of extensive experimental data and then use the model to gain insight into behavior under LWR extended life conditions.

We note that the goals of this work are not to develop a highly quantitative model for precipitation, which is beyond the scope of the project. Our goal is instead to combine what is known from previous models and experiment in whatever ways possible to assess the qualitative features of austenitic 300 series alloy precipitation under irradiation. Our focus is on such issues as time scale for precipitation, radiation enhanced vs. induced formation, and qualitative volume fractions that will dominant the hardening effects. The models we have developed have been quite successful in achieving these qualitative goals and the key results from this work are (for neutron irradiations at 300-400 °C in 316 and 304 SS):

1. Carbide phases are radiation enhanced phases (i.e., their precipitation would occur at equilibrium but the kinetics is enhanced by irradiation) and perhaps also impacted by radiation enhanced dissolution and/or carbon segregation.

2. G-phase and γ' are radiation induced phases (i.e., their precipitation would not occur at equilibrium but radiation induces their formation).
3. Sigma and Laves are kinetically inhibited phases (i.e., they are thermodynamically stable but do not form due to kinetic limitations).
4. Volume fraction of carbide in test reactor measurements is governed by competition of radiation enhanced precipitation and radiation enhanced dissolution. Under LWR conditions, the lower dose rate is expected to weaken the radiation induced dissolution and increase the carbide volume fraction vs. fast reactors for similar dose. Carbide volume fraction may reach up to ~1.2% under LWR conditions for the 316 SS composition we studied.
5. In cold-worked 316 SS the γ' is the dominant radiation induced phase and G-phase is suppressed. γ' nucleates at Frank loops and radiation induced segregation governs the time scale of formation of γ'.
6. At LWR temperature range (~300 °C) the excess vacancies due to irradiation can enhance the substitutional elements diffusion ~10^7 times.
7. In fast reactors temperature range (e.g. 390 °C in Phénix [1]) the M_6C is the dominant phase after 25 dpa, while in LWR conditions (275 °C) the transformation of $M_{23}C_6$ to M_6C is slow and $M_{23}C_6$ is the dominant phase up to 100 dpa. However, these dpa values are quite approximate due to uncertain interfacial energies.
8. If we assume that the radiation induced segregation on dislocations is similar to radiation induced segregation on grain boundaries at LWR conditions, the volume fraction of γ' could reach up to 3.5% in 20 dpa. Again, the dpa value is approximate due to the uncertainties in interfacial energies.

We note that this is the final report on this part of the project so we have included the complete results on this work for easy reference. A paper for publication is also in preparation.

ACKNOWLEDGEMENTS

This research was sponsored by the U.S. Department of Energy, Office of Nuclear Energy, for the Light Water Reactor Sustainability Research and Development effort.

1 Overall approach to modeling precipitation in austenitic stainless steels

Precipitation in austenitic stainless steels (SS) under irradiation is one of the life limiting factors of structural materials in a reactor core. Specifically, precipitation could lead to steel hardening and embrittlement. This situation is more critical under LWR extended life conditions, as there is limited experimental data to address the materials behavior under such low-flux, high-fluence conditions. In the absence of experimental data, modeling techniques can help us to gain insight into materials behavior under LWR extended life conditions.

There are two recent works with an emphasis on thermodynamic and kinetic modeling of austenitic stainless steel precipitates under nuclear power plants conditions. Yang and Busby [2] used the Calphad (Calculation of Phase Diagram) approach and developed a thermodynamic database, OCTANT (ORNL Computational Thermodynamics for Applied Nuclear Technology), for austenitic stainless steels with a focus on reliable thermodynamic modeling of precipitate phases in AISI 316. Then they coupled the thermodynamic database with precipitation kinetics simulation (using MatCalc package [3]) to study the thermal aging of 316 SS. Shim et al. [4] used the same methodology (Calphad database + MatCalc) to study the thermal aging of 316 SS at 400 °C. They also studied the aging behavior of alloys with a radiation induced segregation (RIS) composition to gain insight into radiation induced precipitates (RIP). In both these works authors commented on the lack of radiation enhanced diffusion (RED) and proper dislocation evolution in their modeling as the key missing information which held them back from proper modeling of 316 SS under irradiation. Valid estimation of RED is critical in obtaining correct time scales of precipitation and a realistic dislocation density is necessary both to model the RED and because dislocations serve as nucleation sites for many precipitates in 316 SS under LWR conditions.

To address the aspects lacking in previous works we developed an integrated model which combines the Cluster Dynamics (CD), OCTANT, and MatCalc. We use multiple programs as no one set of codes provides all the necessary modeling tools. The CD model tracks the evolution of defects under irradiation and gives us the evolution of single vacancy (and consequently RED) and total dislocation. The CD predicted RED and dislocation go into MatCalc as input data. For radiation induced phases (RIPs), which occur primarily around dislocation loops, we use a simple model that assumes that RIPs form inside a cylindrical region around the dislocations loops, where this region is assumed to have the appropriate RIS composition. Using the RIS composition to study the RIP is similar to the approach used by Shim et al. [4]. However, in this work, we use the cylindrical model to address the RIP more quantitatively in cold-worked 316 SS (details are given in section 4.4). The developed methodology in this work is general and can be extended to other alloys.

2 Models developed

In this work we develop models for three different irradiation conditions and utilize somewhat different parameters and approaches for each case. To avoid confusion we summarize the conditions, parameters, and approaches here. The three irradiation conditions are

1. Fast reactors at low temperature (9.4×10^{-7} dpa/s and 320 °C).
2. Fast reactors at medium temperature (9.4×10^{-7} dpa/s and 390 °C).
3. PWR conditions at intermediate temperature (1×10^{-7} dpa/s and 343 °C).
4. LWR conditions at low temperature (7×10^{-8} dpa/s and 275 °C).

We model the first set of conditions (section 3.3), to validate the CD model for point defects and loops as there are available several consistent experimental data on loop behavior for these conditions. We model the second set of conditions (section 4.3 and 4.4) to explore the ability to predict precipitation because of the availability of experimental data on precipitation at these and similar conditions. Finally, we model the third and fourth set of conditions (section 5) to gain insight into austenitic steels phase instability and precipitate evolution under the conditions of most importance for practical applications, which are for LWRs under extended life conditions.

The CD model we develop has many parameters taken from the literature but only one fitting parameter that we adjust for to fit specific dislocation loop data sets under specific conditions in this work, which parameter is the binding energy between two interstitials E_{b2i}. For the first set of conditions we find $E_{b2i} = 0.43eV$ as the best fitting parameter to reproduce the experimental loop size and number density. For the second and third set of conditions we find $E_{b2i} = 0.5eV$ and $E_{b2i} = 0.6eV$ best reproduce the experimental loop data. For the fourth set of conditions we find that $E_{b2i} = 0.43eV$ predicts the experimental loop behavior fairly well, which is the same value used for the first set of conditions.

As described in section 1, our general approach is to use the CD model to predict the evolution of the dislocation loop density and vacancy concentration, which are then used as input for sink strength and radiation enhanced diffusion modeling within the MatCalc code. However, for modeling γ' precipitation under the second set of conditions we only use the CD model to predict vacancy concentration, and the dislocations density is taken directly from the mean value of experimental results (see section 4.4).

3 Cluster Dynamics modeling of defects

3.1 Governing equations

Cluster Dynamics (CD) is a computational technique for predicting microstructural evolution and it is frequently applied to precipitation problems or defect cluster evolution in materials under irradiation. In Cluster Dynamics, the system is described as a gas of non-interacting clusters. The clusters are defined by a single parameter, their size (or equivalently, the number of atoms they contain).

In CD modeling of defect clusters the principle of the model is to describe a population of defects by their size distribution. The evolution of these populations is obtained through 'chemical kinetics' in a homogeneous medium, where the probability of a cluster of size n to become a cluster of size $n+1$ or $n-1$ depends on its rate of absorption or emission of a vacancy or an interstitial. These kinetics depend on the available population of mobile defects.

The main parts of the CD model developed here are:

- Rate of defect production from irradiation cascade,
- Recombination rate of point defects,
- Absorption and emission rates of point defects by the defect clusters (loops and voids),
- Annihilation kinetics on fixed sinks like grain boundaries,
- Annihilation kinetics on dislocations and resulting evolution of the dislocation network.

The model will contain a series of coupled ordinary differential equations that capture the evolution of point defects and bigger clusters. The solution of these equations is obtained by direct integration of equations using the CVODE solver [5]. Our approach to building this model will be to use existing models and then alter them as needed to yield agreement with known data on loop evolution.

The modeling approach is taken from references [6-10]. The generation of defects from the cascade is taken from [11] which considers the formation of clusters of size higher than 4 unlikely. The defect generation terms are

$$\begin{aligned} G_i(1) &= \eta G_{dpa}(1 - f_{i2} - f_{i3} - f_{i4}), \\ G_i(2) &= \frac{\eta G_{dpa} f_{i2}}{2}, \\ G_i(3) &= \frac{\eta G_{dpa} f_{i3}}{3}, \end{aligned} \tag{1}$$

$$G_i(4) = \frac{\eta G_{dpa} f_{i4}}{4},$$

$$G_i(n > 4) = 0.$$

Similar expression can be written for $G_v(n)$. G_{dpa} in these equations is the damage rate in the reactor, η is cascade efficiency and f_{in} is the fraction of clusters on size n and type i surviving the reorganization events following the cascade.

Assuming that only monomer defects are mobile the governing equations for defect evolution for clusters bigger than 2 atoms would be as follows [6-10]. Note that in all the equations below we focus on writing the equations for interstitials. Analogous equations exist in each case for vacancies but to avoid having a repetitive document we have left these out. The analogous equations have exactly the same format but the variables would have subscripts of "*v*" for vacancy in place of "*i*" for interstitial and vice-versa.

$$\frac{dC_i(n)}{dt} = G_i(n) + a_{i,n+1}C_i(n+1) - b_{i,n}C_i(n) + c_{i,n-1}C_i(n-1) \qquad n > 2, \tag{2}$$

$$a_{i,n} = \beta_{i,v}(n)C_v(1) + \alpha_{i,i}(n), \tag{3}$$

$$b_{i,n} = \beta_{i,v}(n)C_v(1) + \beta_{i,i}(n)C_i(1) + \alpha_{i,i}(n), \tag{4}$$

$$c_{i,n} = \beta_{i,i}(n)C_i(1), \tag{5}$$

here *i* and *v* refer to interstitials and vacancies (either as point defects or cluster types (i.e., loops and voids, respectively)), the $C_\theta(n)$ is the concentration per lattice site of clusters of type θ (θ can be type interstitial (*i*) or vacancy (*v*)) containing n atoms, $G_\theta(n)$ is the production rate of cluster of size n, $a_{\theta,n+1}$ and $c_{\theta,n-1}$ are the rate of transferring the clusters of size $n+1$ and $n-1$ to cluster n respectively and $b_{\theta,n}$ is the rate of losing clusters of size n.

In these equations the $\beta_{\theta,\theta'}(n)$ and $\alpha_{\theta,\theta'}(n)$ are the rate of absorption and emission of a defect of type θ' by a cluster of type θ and size n respectively and they are defined as

$$\beta_{i,v}(n) = \frac{2\pi r_i(n) D_v Z_v(n)}{V_{at}}, \tag{6}$$

$$\beta_{i,i}(n) = \frac{2\pi r_i(n) D_i Z_i(n)}{V_{at}}, \tag{7}$$

$$\beta_{v,i}(n) = \frac{4\pi r_v(n) D_i Z_i(n)}{V_{at}}, \tag{8}$$

$$\beta_{v,v}(n) = \frac{4\pi r_v(n) D_v Z_v(n)}{V_{at}}, \tag{9}$$

$$\alpha_{i,i}(n) = \beta_{i,i}(n-1)\exp(-\frac{E_{bi}(n)}{kT}), \tag{10}$$

$$\alpha_{v,v}(n) = \beta_{v,v}(n-1)\exp(-\frac{E_{bv}(n)}{kT}), \tag{11}$$

In above equations the $r_\theta(n)$ is the size of the cluster of type θ containing n point defects, V_{at} is the average atomic volume of the steel, T is the temperature, and k is the Boltzmann constant. Critical parameters in the above equations (6-11) are the bias factors $Z_{\theta c}(n)$ of cluster of size n. This bias for interstitial clusters can be defined as (an analogous expression exists for vacancies) [7],

$$Z_{ic} = Z_i + (\sqrt{\frac{b}{8\pi a} Z_{1i}} - Z_i)(1/n^{0.35}), \tag{12}$$

where Z_i is the bias factor for an infinite straight dislocation for the interstitial point defects, a is the lattice parameter, b the Burgers vector and Z_{1i} and a_{1i} are parameters used to describe the evolution of the bias Z_{ic} with the size of the clusters.

The equations 10 and 11, which represent the parameters controlling emission in the CD model, are highly dependent on binding energy. Based on molecular dynamics simulation the binding energies for interstitials in iron can be described by the following expression [12, 13],

$$E_{bi}(n) = E_{fi} + \frac{E_{b2i} - E_{fi}}{2^{2/3} - 1}(n^{2/3} - (n-1)^{2/3}), \tag{13}$$

where E_{fi} is the formation energy of interstitial point defects, n is the number of atom in cluster, and E_{b2i} is the binging energy for a cluster of size two. We will use this parameterization for the present austenitic systems as well. A corresponding expression also exists for vacancies [9].

The evolution equation for monomer interstitial is (an analogous expression exists for vacancies) [8, 9],

$$\frac{dC_i(1)}{dt} = G_i(1) - R_{iv}C_i(1)C_v(1) - \frac{C_i(1) - C_i^e}{\tau_{d,i}^a} - \frac{C_i(1) - C_i^e}{\tau_{gh,i}^a} - \frac{C_i(1)}{\tau_i^a} + \frac{1}{\tau_i^e}, \tag{14}$$

where the R_{iv} is the characteristic annihilation rate of vacancy and interstitial, $\tau_{d,i}^a$ and $\tau_{gh,i}^a$ are characteristics times for annihilation on dislocations and grain boundaries, and τ_j^a and τ_j^e are the characteristic times for absorbing or emitting a defect of type j by the population of interstitial or vacancy clusters of size up to n. These variables can be expressed using the variables above as

$$R_{iv} = 4\pi(D_v + D_i)r_{iv}/V_{at}, \tag{15}$$

$$\frac{1}{\tau_{d,i}^a} = \rho D_i Z_i, \tag{16}$$

$$\frac{1}{\tau_{gb,i}^a} = 6D_i \frac{\sqrt{S_m^i}}{d_g}, \tag{17}$$

$$S_m^i = \rho Z_i + \frac{1}{D_i}\sum_{n=2}^{\infty}(\beta_{i,i}(n)C_i(n) + \beta_{v,i}(n)C_v(n)), \tag{18}$$

$$\frac{1}{\tau_i^a} = \sum_{n=2}\beta_{i,i}(n)C_i(n) + \sum_{n=2}\beta_{v,i}(n)C_v(n) + 4\beta_{i,i}(1)C_i(1), \tag{19}$$

$$\frac{1}{\tau_i^e} = \sum_{n=3}\alpha_{i,i}(n)C_i(n) + 4\alpha_{i,i}(2)C_i(2) + \beta_{i,v}(2)C_i(2)C_v(1). \tag{20}$$

where D_v and D_i are the vacancy and interstitial diffusion coefficients respectively, r_{iv} is the vacancy/interstitial recombination distance, ρ is the network dislocation density, and d_g is the grain boundary size.

Finally, the evolution equation for dimer interstitials (an analogous expression exists for vacancies) is

$$\frac{dC_i(2)}{dt} = G_i(2) + 2\beta_{i,i}(1)C_i(1)C_i(1) - 2\alpha_{i,i}(2)C_i(2) - \beta_{i,i}(2)C_i(1)C_i(2) + \alpha_{i,i}(3)C_i(3) - \beta_{i,v}(2)C_v(1)C_i(2) + \beta_{i,v}(3)C_v(1)C_i(3). \quad (21)$$

Solving the coupled master equations (Eqs. 2, 14, 21) and corresponding equations for vacancies one can capture the evolution of defects clusters during irradiation.

3.2 Parameters for 316 stainless steels

In CD modeling of defect clusters two sets of parameters are needed; 1) material parameters and 2) irradiation parameters. The goal is to find the best set of parameters that successfully reproduce the experimental data, in our case loop size and loop number density. Austenitic stainless steels have been the focus of several studies [9, 14-17]. However, there is no established set of parameters for stainless steel CD models in the literature that cover all the complexity of defect cluster formation in these alloys. The material parameters used in this study are listed in Table 1. In this study we focus on cold-worked 316 SS in order to have a concrete system for comparison. Similar approaches, likely with some tuning of parameters, can be adapted for other processing conditions for 316 SS and for 304 SS.

Table 1. Material parameters for 316 stainless steels.

Parameter	**Value**	**Reference**
Lattice parameter, a_0	3.61 Å	
Interstitial migration energy, E_{mi}	0.2 eV	[14]
Vacancy migration energy, E_{mv}	1.37 eV	[9]
Interstitial pre-exponential, D_{0i}	1.0×10^{-7} m^2/s	[9]
Vacancy pre-exponential, D_{0v}	0.6×10^{-4} m^2/s	[9]
Interstitial formation energy, E_{fi}	4.1 eV	[9]
Vacancy formation energy, E_{fv}	1.61 eV	[18]
Vacancy formation entropy, S_{fv}	$1.73\,k$	[18]
Binding energy of interstitial dimer, E_{b2i}	0.43 eV (at 275 °C, 320 °C), 0.50 eV	Fitting parameter in this work (see Sec. 3.3)

	(at 390 °C), 0.60 eV (at 343 °C),	
Binding energy of vacancy dimer, E_{b2v}	0.5 eV	[9]
Recombination radius, r_{iv}	0.7 nm	[9]
Dislocation density, ρ_0	1×10^{14} m^{-2}	[9]
Average grain size, d	40 μm	[9]
Burgers vector of the loop assumed to be prismatic, b	$a/\sqrt{3}$	[15]
Capture efficiency for interstitial by dislocation net, Z_i	1.1	[9]
Capture efficiency for vacancy by dislocation net, Z_v	1.0	[9]
Z_{1i}	42.0	[9]
Z_{1v}	35.0	[9]

The other set of parameters is the irradiation parameters. These parameters characterize the irradiation conditions, which include the environmental parameters, e.g. temperature, damage rate and the in-cascade clustering behavior of the target material. Table 2 shows the irradiation parameters used in this work.

Table 2. Irradiation parameters used in CD-defect model.

Parameter	**Value**	**Reference**
Temperature, T	275 °C, 320 °C, 343 °C, 390 °C	See text for references of specific values
Dose rate, G_{dpa}	7×10^{-8}, 1×10^{-7}, 9.4×10^{-7} dpa/s	See text for references of specific values
Damage efficiency, η	0.15	[9]
Dimer interstitial fraction in cascade, f_{i2}	0.2	[9]

Trimer interstitial fraction in cascade, f_{i3}	0.2	[9]
Four-interstitial fraction in cascade, f_{i4}	0.06	[9]
Dimer vacancy fraction in cascade, f_{v2}	0.06	[9]
Trimer vacancy fraction in cascade, f_{v3}	0.03	[9]
Four-vacancy fraction in cascade, f_{v4}	0.02	[9]

3.3 CD results and predictions for dislocation density and vacancy concentration

By solving governing equations in section 3.1 along with parameters in section 3.2 we are able to capture the loop evolution in 316 SS under neutron irradiation. We fit the model with three sets of experimental data, which are chosen for the following reasons. First, these experiments are all conducted at 320 °C under neutron irradiation, making them highly relevant for LWR conditions. Furthermore, these studies go to quite high doses (up to 30 dpa), so large dose effects can be captured. Finally, these experiments also were all conducted at the BOR-60 reactor, so the data are expected to be more consistent than samples collected from more varied environments. Figure 1 shows the evolution of loop size and number density in 316 SS under neutron irradiation at 320 °C from these three experimental data sets, along with our modeling result.

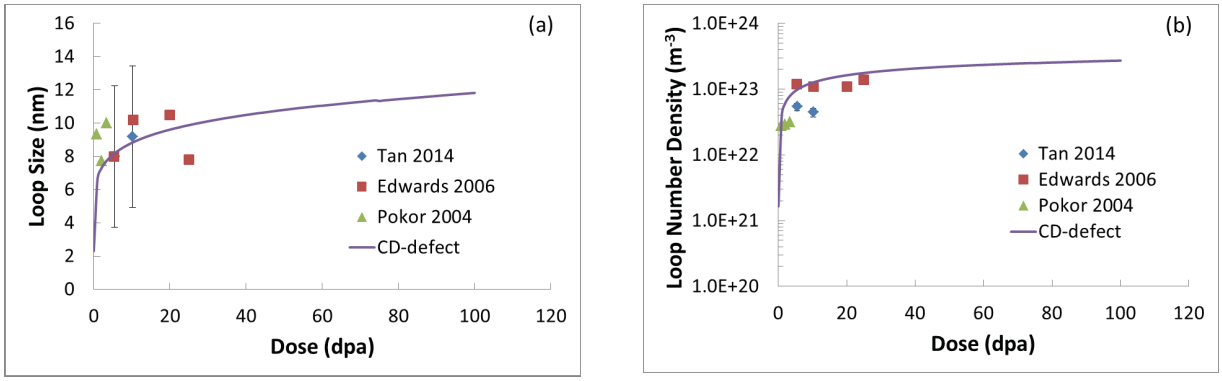

Figure 1. Loop size (a) and loop number density (b) evolution in 316 SS at 320 °C under 9.4×10^{-7} dpa/s neutron irradiation.

Our CD modeling of defect evolution uses just one fitting parameter, E_{b2i}, while the other parameters are selected from literature, as shown in Table 1 and Table 2. Pokor et al. [9] reported the interval of 0 to 2 eV for E_{b2i} as an acceptable interval based on experimental data available

in the literature. We gridded the 0 to 2 eV space and found $E_{b2i} = 0.43\ eV$ as the best value to reproduce the loop sizes and number density in Figure 1.

After finding the appropriate parameters for the CD model to reproduce the loop size and number density evolution, we use the CD model to predict the evolution of single vacancy and total dislocation concentrations, as these are critical for modeling precipitation. The single vacancy and total dislocation concentrations were then fit with simple functional forms, which were incorporated into the precipitation model as input data. Extra single vacancies generated during irradiation will enhance the diffusion of substitutional elements as following [19],

$$D_X^{irr} \approx [D_V C_{1V}^{irr}]\frac{D_X^{th}}{D_{sd}^{th}} + D_X^{th} \approx (\frac{C_{1V}^{irr}}{C_{1V}^{th}} + 1)D_X^{th} \approx \frac{C_{1V}^{irr}}{C_{1V}^{th}} \times D_X^{th}, \quad (22)$$

where D_X^{irr} (D_X^{th}) is the radiation enhanced (thermal) diffusion coefficient of element X, D_V is the diffusion coefficient of vacancy, C_{1V}^{irr} (C_{1V}^{th}) is the concentration of single vacancies under irradiation (thermal equilibrium) and D_{sd}^{th} is the self-diffusion coefficient. In addition, irradiation induced faulted loops increase the nucleation sites for those phases that nucleate at dislocations. Figure 2 shows the evolution of single vacancy and total dislocation concentrations and their curve fitted functions versus time (in seconds). We note that in adopting these curves for use in our simulations we are assuming that the CD model results can be applied in the complete alloy simulation. In particular, this assumes that the precipitates do not significantly impact the defect concentrations. This is a reasonable approximation given the generally low precipitate concentrations in these alloys [20-22].

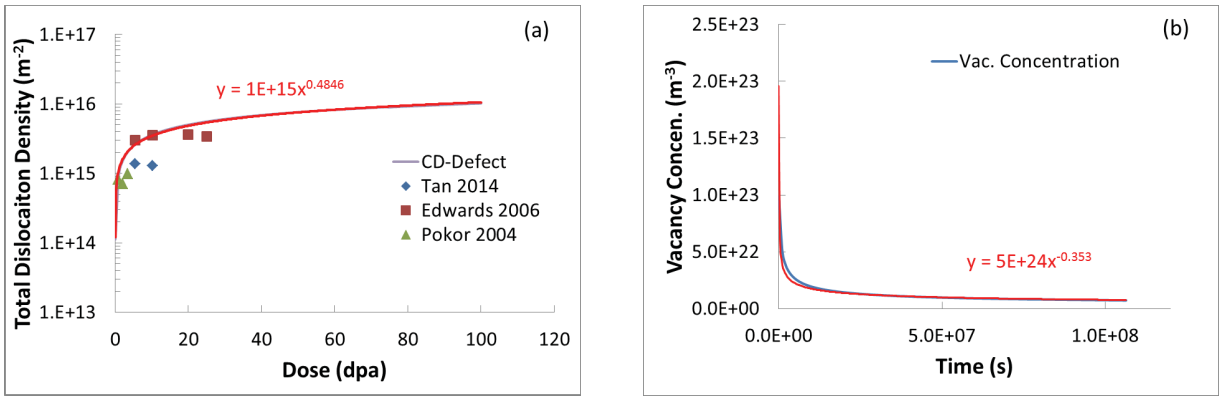

Figure 2. Evolution of total dislocation density (a) and single vacancies concentration (b) in 316 SS at 320 °C under 9.4×10^{-7} dpa/s neutron irradiation. Note that the CD model results (CD-Defect) are under the fitted red line in figure (a).

4 Precipitation in 316 stainless steels under irradiation

4.1 Thermodynamics

To capture the thermodynamics of 316 SS we use OCTANT (ORNL Computational Thermodynamics for Applied Nuclear Technology) database [2, 23, 24]. OCTANT includes Fe, C, Cr, Ni, Mn, Mo, and Si with a focus on thermodynamic modeling of AISI 316 austenitic stainless steels. In this work we use the same material composition as used in reference [1]. The chemical composition of the alloy we will model is listed in Table 3. Minor alloying elements like P, S, Cu, Al, B, Nb, and Ti were not considered in this work.

Table 3. Chemical composition (wt.%) of 316 SS [1].

Alloy	Fe	Cr	Ni	Mn	Si	C	Mo
316 SS	Bal.	16.6	10.6	1.12	0.68	0.054	2.25

For the composition in Table 3 OCTANT predicts α ferrite at low temperatures [2]. However under routine processing conditions of austenite steels, the presence of α ferrite in the microstructure is rare, presumably due to kinetic limitations. Therefore, we suspend α ferrite in the phase calculations. Figure 3 shows the calculated equilibrium phases and their mole fractions, without α ferrite, in 316 SS from 200 °C to 1500 °C.

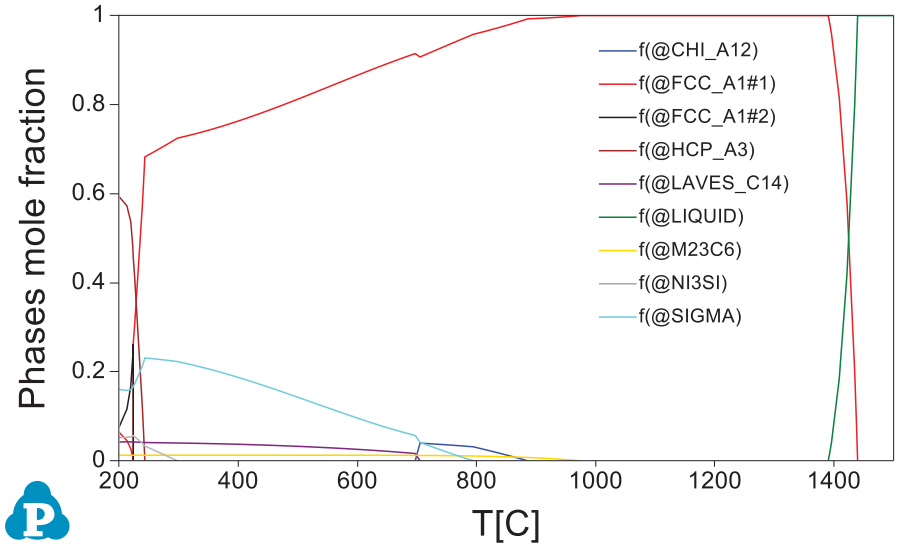

Figure 3. Calculated equilibrium phase mole fraction vs temperature (°C) for 316 SS.

The phase fraction study (Figure 3) shows that FCC (austenite), Sigma, Laves, and $M_{23}C_6$ are stable phases at temperatures around 300 °C. However, reported experimental data on precipitates in 316 SS under irradiation at LWR temperature range (~ 300 °C) do not show

Sigma and Laves phases [1, 21, 25-28]. This fact indicates that Sigma and Laves are kinetically inhibited phases in 316 SS under LWR conditions. We note that the low temperature data is exclusively from Calphad predictions and no validation has been done at temperatures lower than 400 °C. For convenience we provide a summary of the volume fractions of precipitates we have extracted from the literature in section 10.

4.2 Kinetics

We combine the thermodynamics from Sec. 4.1 with the radiation defects modeling from Sec. 3.3 to determine the precipitation behavior in 316 SS under irradiation. For the kinetics part of the study we use the thermo-kinetic software package MatCalc developed by Kozeschnik et al. [3]. MatCalc treats the kinetics of microstructural processes based on classical nucleation theory and evolution equations for the radius and composition of each precipitate derived from the thermodynamic extremum principle [29].

Precipitation simulation needs four sets of data as input; 1) thermodynamic property database, 2) mobility database, 3) interfacial energies, and 4) microstructure information (specifically, precipitate nucleation sites). For the thermodynamic database we used OCTANT and for the mobility database we used MatCalc mobility database (mc_fe2.006) for steel, which contains elements mobility data for face-centered-cubic (FCC) and body-centered-cubic (BCC) steels. Interfacial energies for the interface of precipitate and matrix depend on degree of coherency, crystallographic misorientation, elastic misfit strains, and solute segregation. Because of this complexity, interfacial energy generally cannot be reliably enough measured from direct experiment or calculated from atomistic methods and it is usually treated as a fitting parameter in precipitation modeling. MatCalc uses a generalized nearest-neighbor broken bond (GNNBB) model for calculation an estimate of the interfacial energy [30] and we use these default values for our present, mostly qualitative, models. Finally, the microstructure information, specifically the initial dislocation density and grain size depend on heat treatment history of individual alloys and we use the values from Pokor et al. [9] which are given in Table 1.

To incorporate the effect of irradiation on precipitation we modify the MatCalc input parameters from those for thermal aging modeling to include CD-predicted RED and dislocation density, which we briefly discuss here. The RED is included by adding in the effects of excess vacancies from radiation on elemental diffusion. We assume the elemental diffusion is dominated by vacancies. Therefore, the diffusion enhancement factor can be calculated by the function in Figure 2 (b) and applying Eq. (22). The challenge of including dislocation density is that generally, in precipitation under aging, the background dislocation is assumed to be stationary, which means the number of nucleation sites is unchanging during precipitation. This assumption is not correct for materials under irradiation as the Frank loops, induced by irradiation, are evolving and consequently nucleation sites are changing with time. Thus, the function in Figure 2 (a) is used to define time dependent matrix dislocation properties in MatCalc

Experimental observations report the formation of carbide phases (including $M_{23}C_6$ and M_6C), γ' and G-phase in standard 316 SS under LWR conditions [1, 20-22, 25, 31, 32] (further data provided in section 10). Among these phases, carbides are the most common second phases in stainless steels and they form easily under aging [2]. Unlike carbides, γ' and G-phase have not been observed in standard 316 stainless steels under thermal aging. These phases are generally Ni-Si rich clusters which form because of radiation induced segregation of Ni and Si to sinks (dislocations, grain boundaries, voids surfaces etc.). In the sections below we first discuss the precipitation of carbides and then the γ' and G-phase.

4.3 Carbides

Formation of carbides in stainless steels is well established. $M_{23}C_6$ is one of the first precipitate phases that show up in 316 SS under aging [33] and its thermodynamics has been extensively studied at high temperatures [33, 34].

A question of some interest to the community is how we expect radiation to enhance carbide kinetics, if at all. Excess vacancies introduced by irradiation enhance the diffusion of substitutional elements and have minor effect on interstitial atoms. In $M_{23}C_6$ the M sublattice includes substitutional elements (Cr, Fe, Mn, Mo, Ni) but carbon comes from interstitial sites. Therefore, radiation induced excess vacancies only enhance the M sublattice elements in $M_{23}C_6$. Diffusion coefficient databases show that carbon is the fastest diffusing element in 316 SS under thermal aging [35] and consequently the kinetics of precipitation of carbide phases is controlled by M elements, which are the slowest diffusers in the compound. Under irradiation the mobility of M elements increases dramatically, which means that carbides formation kinetics is expected to be enhanced by irradiation. However, it is important to assess whether carbon is still the fastest diffusing element in the carbides under irradiation, as the extent of the radiation enhancement will be reduced if carbon becomes the limiting element, since it is not impacted significantly by the irradiation. To estimate the enhancement of M elements we note that the concentration of excess single vacancies under irradiation converges to ~10^{22} m^{-3} based on Figure 2. At 320 °C the thermal concentration of single vacancies is about 10^{16} m^{-3} ($C_{1V}^{eq} = \exp(S_{fv}/k)\exp(-E_{fv}/kT)$ where S_{fv} is the vacancy formation entropy, E_{fv} is vacancy formation energy, k is Boltzmann constant, and T is temperature – see Table 1 for values). Comparing the vacancy concentration under irradiation and thermal aging shows that irradiation will enhance the diffusion coefficients of substitutional elements by a factor of ~$10^{22}/10^{16}=10^6$. Table 4 shows the thermal and irradiation enhanced diffusion coefficient of carbon and M elements (Cr, Fe, Mn, Mo, Ni) in 316 SS at 320 °C. Diffusion coefficient data under irradiation show that the radiation enhanced diffusivity of M elements are still less than carbon, which indicates that M elements will still control the kinetics of carbide formation under irradiation at 320 °C and 9.4×10^{-7} dpa/s. For LWR conditions the neutron flux is lower than 9.4×10^{-7} dpa/s, which is expected to even further reduce M diffusion versus carbon. Therefore, the carbide

formation kinetics is expected to be enhanced by radiation, and the enhancement is expected to arise from the total enhancement of the transport of the metal atoms, without additional limiting factors associated with C.

Table 4. Diffusion coefficient of carbides components in 316 SS at 320 °C (from MatCalc mobility database, mc_fe2.006).

Element	Tracer diffusion coefficient at FCC (m^{-2}/s)	Radiation enhanced diffusion (m^{-2}/s)
C	6e-20	6e-20
Cr	1e-29	1e-23
Fe	9e-30	9e-24
Mn	8e-29	8e-23
Mo	2e-29	2e-23
Ni	2e-30	2e-24

By incorporating enhanced diffusion of M atoms and dislocation evolution (which alters heterogeneous nucleation sites) in our thermo-kinetic model, we are able to model the carbides precipitation under irradiation. Since we have better experimental data on carbides precipitation at temperature around 390 °C [1, 25, 26, 28] we focus on this temperature range. The CD model, that we developed and parameterized in Section 3, needs to be refitted to match the loop size and loop number density (at 390 °C) reported in Ref. [1]. Figure 4 and Figure 5 show the predictions for the refit model compared to the experimental results.

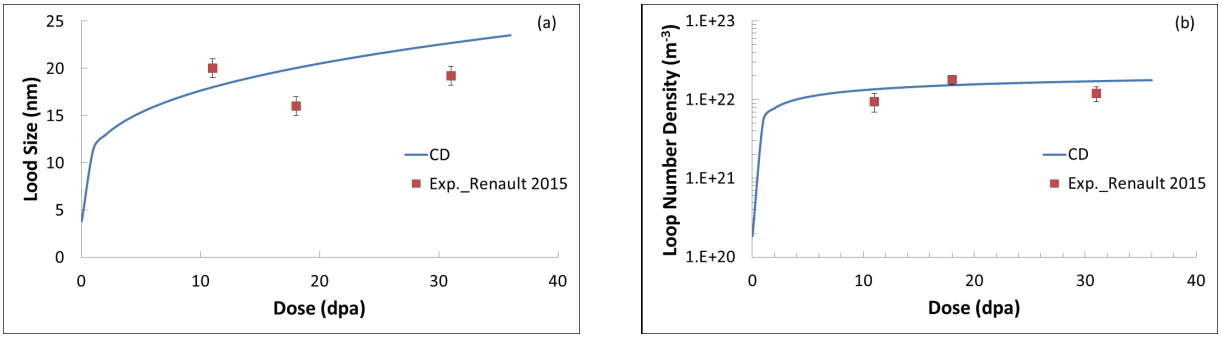

Figure 4. Loop size (a) and loop number density (b) evolution in 316 SS at 390 °C under 9.4×10^{-7} dpa/s neutron irradiation (experimental data are from Ref. [1]).

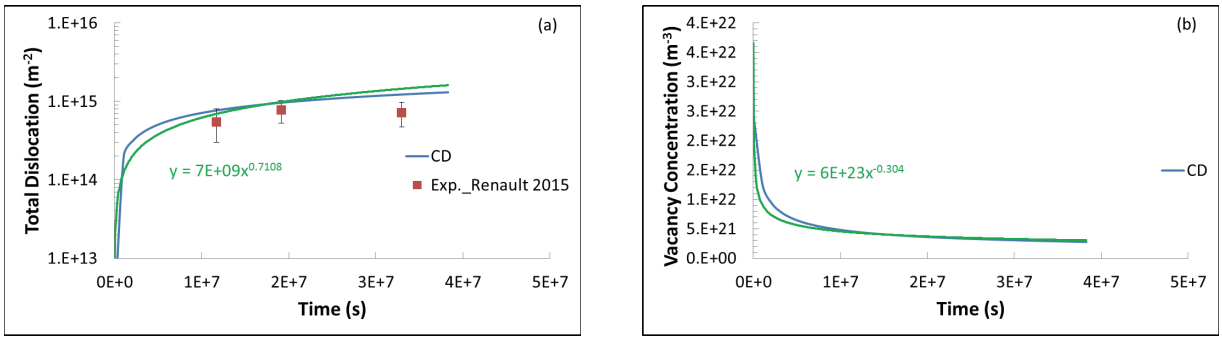

Figure 5. Evolution of dislocation density (a) and single vacancies concentration (a) in 316 SS at 390 °C under 9.4×10^{-7} dpa/s neutron irradiation (experimental data are from Ref. [1]).

We find that $E_{b2i} = 0.5$ eV can reproduce the experimental results well. It is not likely that 70 °C change in temperature would actually change E_{b2i} 0.07 eV. We assume this difference is due to the fact that this fitted energy is compensating for other changes with temperature that the CD model does not capture. Figure 6 shows both modeling and experimental data of carbides volume fraction in 316 SS at a range of temperatures lower that 400 °C under radiation (9.4×10^{-7} dpa/s). Most experimental data show very low carbide volume fraction even up to 100 dpa. In addition to the reported data in Figure 6, Tan et al. [20] and Edwards et al. [21] also reported very small nanoscale carbide precipitates under irradiation at BOR-60 at 320 °C, which further supports the result that there is very little carbide precipitation under irradiation.

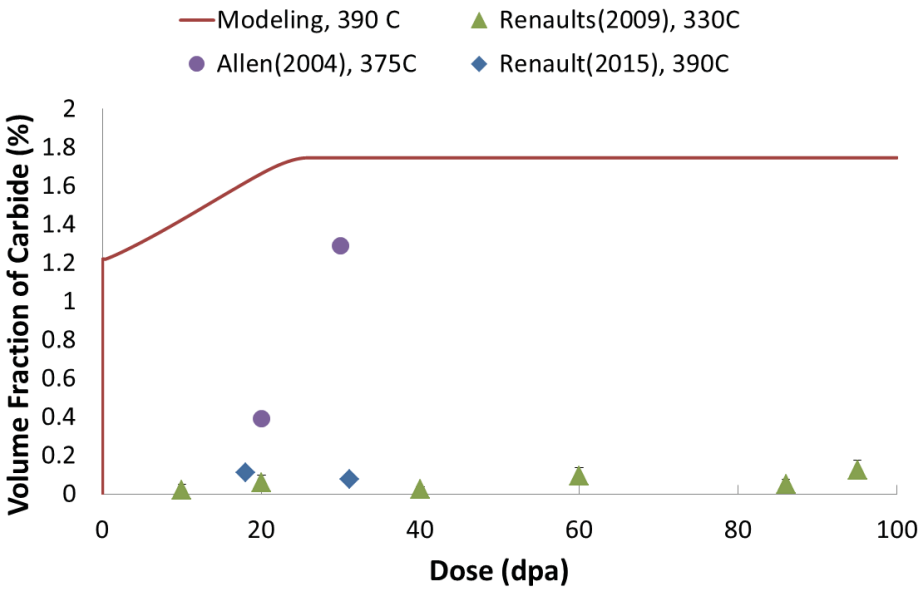

Figure 6. Evolution of total carbides ($M_{23}C_6$ + M_6C) volume fraction compared to experimental data [1, 25, 28] (modeling dose rate = 9.4×10^{-7} dpa/s).

Comparing the volume fraction of carbides predicted by CD-informed thermo-kinetic model with experimental data generally shows an order of magnitude difference. Modeling under the conditions of Figure 6 predicts a very rapid fast formation of a 1.2% volume fraction $M_{23}C_6$ (this phase saturates within ~0.1 dpa), which then gets replaced gradually by M_6C while increasing to a final volume fraction of 1.7%. Formation of M_6C has been reported at high temperature (650 °C) aging of 316 SS [33]. Goldschmidt proposed that M_6C may form through reaction of $M_{23}C_6$ with Mo as follows [36],

$$M_{23}C_6 \xrightarrow{+Mo(650\,^{\circ}C/1500\,hr)} (Fe,Cr)_{21}Mo_2C_6 \xrightarrow{+Mo} M_6C$$

Despite the high volume fraction of carbide in modeling, the bulk of experimental data show a steady state volume fraction in the order of 0.1%. The exception is the data of Allen et al. [28], particularly the value at ~30 dpa, which shows a volume fraction of about 1.3% (all precipitate formation percentages are given as volume fractions in this report unless otherwise labeled). MatCalc calculates the molar fraction of precipitates. We convert the outputs of MatCalc to volume fraction by using the relations provided in section 9. While we cannot presently be sure of the explanation of the differences in this data vs. other experiments, it is observed that the highest value is comparable to the values predicted by our model.

We note that for carbide precipitation we use the initial 316 SS bulk composition and ignore the effect of RIS on bulk composition. This approximate is reasonable because the carbide forms very quickly on the timescale of the RIS, which takes tens of dpa to saturate. However, one effect of RIS on carbide could be a shift in $M_{23}C_6$ to M_6C transformation. Aging studies suggest that carbide forms on dislocations and grain boundaries [33]. After carbide formation, the composition at these dislocations and grain boundaries would gradually change due to RIS. Specifically, RIS would deplete the Mo at sinks (Table 5) which is believed to facilitate the $M_{23}C_6$ to M_6C transformation [33, 36]. Therefore, the $M_{23}C_6$ to M_6C transformation might become slower due to Mo depletion through RIS.

To determine the source of the discrepancy between the model and experiments we first considered possible errors in the model thermodynamics. We benchmarked our thermodynamic database against aging experimental data at high temperatures where kinetics allows the system to reach equilibrium. The key question we seek to answer is whether the carbide saturation level of volume fraction (1.2-1.7%) is reasonable or not. It is well known that $M_{23}C_6$ is the first emerging second phase in 316 SS during aging and it reaches to its saturation level fairly fast [33]. The saturation level of carbides is also known experimentally to vary between 1-2 wt.% depending on carbon initial concentration [34]. Given that our irradiation experiments are at lower temperature than the experiments in Ref. [34] (this reference has several aging experiments in the range of 600-700 °C) we expect similar or higher concentrations of carbides at equilibrium. Therefore, our rapid formation of 1.2% carbide followed by additional growth to 1.7% is not surprising, and in fact is quite consistent with what is known about carbide

precipitation thermodynamics. It is therefore the low volume fraction of carbides in the irradiation experiments that are surprising.

We have thought of four possible mechanisms which may cause the discrepancy we observe between the experimental and modeling results, which mechanisms are

1. In the experimental period observed the carbide does not reach equilibrium due to slow kinetics.
2. Formation of other phases, e.g. γ' and G-phase, suppress the carbide.
3. Irradiation changes the spatial distribution of carbon alter or suppress carbide nucleation and growth, leading to less carbide and/or harder to detect small carbides.
4. Carbide particles are dissolved by irradiation.

The first mechanism is unlikely as experiments go up to very high doses (e.g., 100 dpa), so it is hard to believe that a radiation enhanced phase, like the carbides, does not reach to its equilibrium under the experiments. The second mechanism is also unlikely as our kinetics simulation with RIS composition, where the γ' and G-phase can form, shows formation of ~ 1.2% carbide. Shim et al. [4] also reported the formation of carbide in RIS regions [4], suggesting the RIS induced phases do not suppress the carbide.

We believe the third and/or fourth hypothesis could be the causes behind low experimental and high modeling volume fraction of carbide. In support of the third mechanism, Jiao and Was [37] reported that carbon will deplete at grain boundaries under proton irradiation. Hatakeyama et al. [38] also showed that carbon will deplete at dislocations under neutron irradiation. On the other hand, thermal aging experimental studies showed that carbides prefer to nucleate at grain boundaries and dislocations [33]. Therefore, we can conclude that since irradiation pushes carbon away from the preferred sites for carbides, e.g. dislocations and grain boundaries, the ability to nucleate new carbides or grow existing ones may be suppressed under irradiation. This suppression dislocations and grain boundaries may reduce the total carbide precipitation and/or shift carbides to nucleate more homogeneously, which will likely lead to the formation of smaller precipitate particles that are harder to detect experimentally.

Radiation enhanced dissolution, the fourth mechanism above, also may be the cause of discrepancy between the model and experimental results. Similar to modeling results, experimental results show that carbide saturate at the very beginning of irradiation. This fact indicates that carbide phases under irradiation at fairly low temperatures ranges (e.g. LWR temperature range) will quickly reach a steady state, consistent with our prediction of rapid kinetics for the carbides. However, this steady state does not appear to be thermodynamic equilibrium. To understand this steady state we note that irradiation qualitatively affects the phase formation and stability in two opposite ways; 1) it enhances the precipitation by increasing the diffusion of elements in matrix; 2) it dissolves the precipitates through recoil dissolution and disordering dissolution [39]. Competition between these two effects provides a steady state

situation for precipitate phases that is not thermal equilibrium. Enhancing and dissolving effects of irradiation guide precipitate particles to an optimum size. Precipitates smaller than the optimum size will grow and precipitates larger than this size will shrink. The latter effect is sometimes called radiation induced reverse Ostwald ripening. We propose that radiation enhanced dissolution is the main reason that carbides do not reach thermal equilibrium at fast reactors at 300-400 °C. In other words, we propose the dissolution effects, which are not presently in our model, are the reason for the above discussed discrepancies in predicted (and measured at high-temperature) thermal equilibrium carbide volume fraction and low-temperature irradiation induced carbide volume fraction. While further work is needed to verify this hypothesis we note that carbides dissolution under irradiation was experimentally observed in PE16 alloys [40]. The role of this dissolution may depend strongly on many factors (composition, temperature, etc.) but particularly flux, making it a critical area for further research given the use of high-flux accelerated testing methods in many studies of microstructure evolution.

This explanation may help us to understand the Allen et al. [28] data points. The dose rate in Allen's experiment is 1×10^{-7} dpa/s while the Renault's experiments were conducted at 9.4×10^{-7}, 8.7×10^{-7}, and 5.3×10^{-7} dpa/s. All these three experiments were done on cold-worked 316 SS and although Allen et al. did not mention the initial concentration of carbon we know that the typical 316 SS have maximum 0.1 wt.% carbon [34]. Renault's 316 SS had 0.06 wt.% carbon. Based on available aging experimental data [34], it is unlikely that 0.04 wt.% difference in carbon concentration could cause 12 times higher carbide precipitate, i.e. the values seen for 30 dpa in Allen et al.. The aging experimental data show that 0.05 wt.% higher carbon can increase the carbide precipitate level by about three times (from 0.7wt.% to 2wt.%) [34]. In addition, the experiments of Allen et al. differ by just 15 °C from Renault et al., which suggests temperature difference is not expected to have a large effect on the total steady state carbide volume fraction. Therefore, even if we assume that Allen's alloy had the highest likely initial carbon, its carbide level is not expected to be 12 times higher that Renault's alloy. The most obvious difference between these experiments which might explain the different volume fractions is the dose rate. Renault's dose rate for the data point at 30 dpa is 8.7×10^{-7} dpa/s, while Allen's dose rate is 1×10^{-7} dpa/s. This difference suggests that the lower dose rate experiment of Allen leads to weaker radiation enhanced dissolution than Renault, and therefore larger precipitate volume fractions that appear to take longer to reach steady state. However, it is also possible that Allen's samples were exceptionally high in initial matrix carbon.

4.4 γ′ and G-phase

γ' is an ordered FCC phase ($L1_2$, F_{m3m}) with almost similar lattice parameter as austenite and little or no misfit. The γ' stoichiometric atomic composition is Ni_3X where X typically is Si, Nb, or Al [41]. Morphologically, γ' was observed as small spheres in the matrix [42].

G-phase also has a FCC crystal structure (*A*l, F_{m3m}). It is a complex silicide with stoichiometric atomic composition of $M_6Ni_{16}Si_7$ where M can be Cr, Fe, Mn, Mo, and Ti. G-phase has 1.1 nm lattice parameter and its unit cell contains 116 atoms. Morphologically, G-phase was observed as small rods [42].

Aging studies of 316 SS have shown that γ' and G-phase are not thermally stable phases in standard 316 SS at temperatures where they are often seen, so they are categorized as radiation induced phases [43]. The main driving force for formation of γ' and G-phase is radiation induced segregation (RIS). In typical 316 SS the level of Si is low enough (~0.7 wt.%) to prevent formation of γ' and G-phase. However, under irradiation the Si and Ni enrich at sinks (e.g. dislocations) and these excess Si and Ni in RIS regions facilitate the formation of γ' and G-phase. Segregated elements at sinks change the alloy composition in these regions to such an extent that those regions can be approximately considered as different alloys. In fact, in some literature the term "microalloys" is used for RIS regions [44]. Table 5 shows the typical composition of RIS enhanced "microalloy" regions in 316 SS at 5 dpa, 10 dpa, and 20 dpa.

Table 5. Typical composition of radiation induced segregation regions for 316 stainless steels (wt.%) [4].

	Fe	Cr	Ni	Mo	Mn	Si	C
RIS composition at 5 dpa	Bal.	14±2	18±2	1	1	3±2	0.05
RIS composition at 10 dpa	Bal.	12±1	21±4	1	1	5±1.5	0.05
RIS composition at 20 dpa	Bal.	11±2	24±2	1	1	6	0.05

In this study we focus on precipitation behavior of cold-worked 316 SS as they have been studied extensively experimentally. In experimental observations it is generally reported that the γ' is the dominant phase in cold-worked 316 SS and G-phase is almost suppressed [1, 20, 21, 25]. We believe that the suppression of G-phase in cold-worked 316 SS is due to the fact that it competes with γ' for both Ni and Si, and that in cold-worked materials the initial large dislocation density and associated RIS stabilizes γ', which then destabilizes G-phase. A perfect model would reproduce these kinetic effects but unfortunately our model still predicts significant G-phase for cold-worked 316 SS under relevant irradiation conditions. We believe that this discrepancy is due to our interfacial energy for G-phase being too small, and therefore its nucleation kinetics is too fast. As noted above in Sec. 4.2, our interfacial energies are determined by a simple method which one cannot expect to be quantitative. Given the limited data, fitting the interfacial energy of G-phase is likely not practical at this point. Therefore, we simply suspend the G-phase in our modeling of the kinetics of cold-worked 316 SS. However, we note that the tools we have developed here can easily be applied to other situations where G-phase might form, although a refinement of the interfacial energy, likely to larger values that we have

used, may be needed. Transmission electron microscopy (TEM) observations also show that γ' nucleates at Frank loops and it is well distributed in the matrix. Since the radiation induced segregation is necessary to form γ', we can conclude that γ' forms in the matrix of "microalloys", i.e., the RIS region around dislocations. Note that we do not consider the RIS and "microalloys" around grain boundaries as their contribution to the sink density is negligible compared to that from the dislocations. Figure 7 shows schematically the RIS cylinder (or tubular) region around a dislocation line. The diameter of the RIS cylinder for Si (which is the key element for formation of γ' [4]) in neutron irradiated 316 SS was measured to be around 4 nm [38].

Figure 7. Schematic representation of RIS cylindrical (or tubular) region around a dislocation and its mapping to a mean field model.

The ability to model an alloy with a RIS microalloy environment around dislocations is not presently available in the MatCalc code that we are using to model precipitation (see Sec. 4.2) and recoding to rigorously treat this situation is beyond the scope of the present project. Therefore, we have taken an approximate approach to modeling the precipitation, which is to simulate the precipitation in the RIS region by using just the RIS "microalloy" environment in MatCalc. In other words, to study the RIS region we study a bulk material with the RIS composition and an appropriate dislocation density and RED. A similar approach was taken by Shim et al. [4] for modeling radiation induced phases in 316 SS. However, we extend their approach by including the dislocation density and radiation enhanced diffusion from the models we have developed (see Sec. 3.3), which enables us to capture the γ' more quantitatively. The dislocation density for our "microalloy" model must be adjusted to correspond to that in the standard mean-field representation used in MatCalc (see Figure 7b) which can be determined as: $\rho = \pi D_{loop} / (\pi D_{loop} \cdot \pi r_{Cyl}^2) = 1/\pi r_{Cyl}^2 \sim 8 \times 10^{16}\ m^{-2}$.

There are at least two major approximations associated with our "microalloy" approach. First, while we can take RIS composition from experiments, it is actually a function of time. Since our model cannot capture the continuous change of RIS "microalloy" composition we assume that the composition is fixed at each dpa, with values taken from experiments (or interpolation between the experiments). This assumption will not affect the results significantly as the kinetics of γ' is very fast enough compared with RIS evolution time scale, so we can approximately take RIS as fixed for any given simulation of γ' evolution. Figure 8 shows the kinetics of γ' precipitation inside the RIS region, which indicates that the γ' reaches to its

equilibrium level within 0.01 dpa. This value is much lower than that needed for any major compositional change due to RIS, which typically takes tens of dpa to saturate.

The second approximation comes from the assumption that the γ' formation is shut down by the depletion of local enhanced concentrations (primarily Si). This approximation is again reasonable due to time scales. Because the γ' formation takes place over ~0.01 dpa and is driven by the RIS enhanced "microalloy" composition which evolves over tens of dpa, it is expected that the γ' will precipitate until the local "microalloy" supersaturation is depleted.

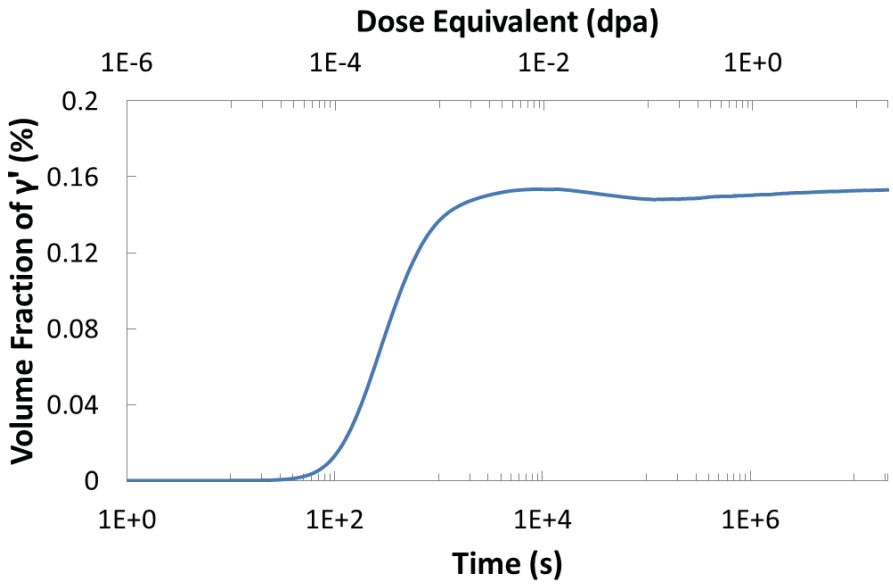

Figure 8. Kinetics of γ' inside the RIS region under 9.4×10^{-7} dpa/s at 390 °C (The domain composition is the RIS composition at 5 dpa from Table 5).

Modeling the kinetics of precipitation in "microalloys" with the OCTANT database and MatCalc will give us the volume fraction of γ' inside the cylinder shown in Figure 7. In our calculations we consider the asymptotic volume fraction of γ' due to its fast precipitation process. To obtain the total volume fraction of γ' in austenite matrix we must multiply the obtained γ' volume fraction with the volume fraction of RIS regions (which comes from loops size and number density) as follows

$$V_{f,\gamma'}^{Aus} = V_{f,\gamma'}^{RIS} \times V_{f,RIS}^{Aus}, \tag{23}$$

here $V_{f,\gamma'}^{Aus}$ is the volume fraction of γ' in austenite, $V_{f,\gamma'}^{RIS}$ is the volume fraction of γ' in RIS regions, and $V_{f,RIS}^{Aus}$ is the volume fraction of RIS regions in an austenite matrix. $V_{f,RIS}^{Aus}$ can be calculated as following,

$$V_{f,RIS}^{Aus} = \pi D_{Loop} \times \pi r_{Cyl}^2 \times N_{Loop}, \quad (24)$$

where D_{Loop} is the average diameter of loops (so πD_{Loop} is the loop length), r_{Cyl} is the radius of RIS regions width (which is ~2 nm [38]), and N_{Loop} is the number density per unit volume of loops.

We use the RIS compositions in Table 5 with some linear interpolation/extrapolation, when needed, and experimental loop data from reference [1] to predict the evolution of γ' in cold-worked 316 SS under irradiation. We need to emphasize that we do not use the loop size and loop number density of the CD model in section 3, because the volume fraction of γ' is linearly dependent to the loop number density (Eq. 23 and 24) and the experimental loop number density usually has a wide error bar range, e.g. in Ref. [1] the upper bars are four to six times larger than lower bars. Therefore, even a perfect CD model, which is in the error bar range, may give a two or three times different magnitude for volume fraction of γ'. Therefore, we use the mean values of experimental loop size and number density for cold-worked 316 SS from Ref. [1], as shown in Figure 9, to benchmark our "microalloy" methodology without having additional uncertainties associated with our model loop size and number density.

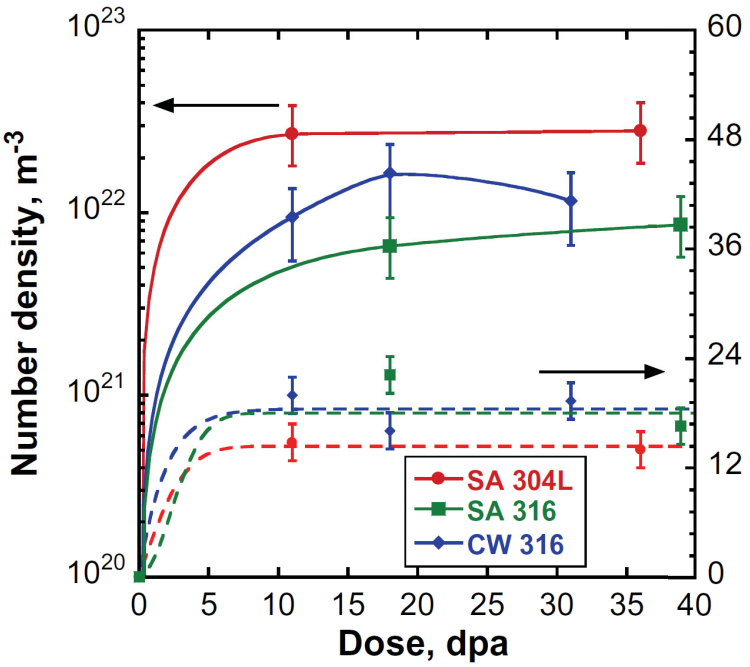

Figure 9. We use the mean values of experimental loop size and loop number density for cold-worked 316 SS (blue line) in quantitative modeling of γ' precipitation (from Ref. [1]).

Using the described methodology in above, we track the evolution of volume fraction of γ' under irradiation. Figure 10 shows the comparison between predicted γ' volume fraction evolution and the experimental data. The average dose rate of experimental study is 9.4×10^{-7} dpa/s and irradiation was conducted at 390 °C. The results show a good agreement between the experimental data and the integrated model (CD + Calphad + MatCalc) predictions.

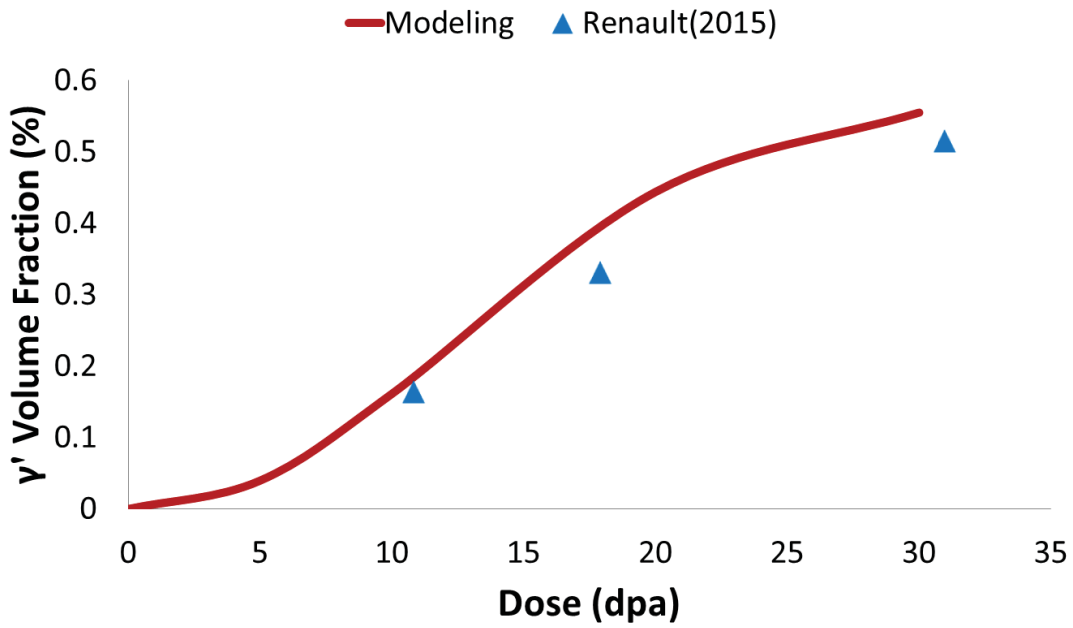

Figure 10. Comparison between modeling predictions and experimental data [1] of γ' volume fraction evolution under 9.4×10^{-7} dpa/s irradiation at 390 °C in CW 316 SS. The plot is produced based on this assumption that the elements segregation to dislocation is similar to grain boundaries.

5 Extrapolation of the model to LWR conditions

The integrated model (CD + Calphad + MatCalc) described in preceding sections was mainly developed for fast reactors where a fairly wide range of experimental data are available. Unfortunately, the experimental database for post-irradiation microstructural examination of austenitic stainless steels under LWR conditions is insufficient to aid in verification of such model. Specifically, there is no experimental data for LWR under extended life condition. The developed model can therefore be used to gain insight into the less well explored domains of austenitic stainless steels degradation under LWR conditions, especially under extended life conditions. Light water reactors operate at relatively low temperature range, i.e. 275-340 °C and low dose rate $(2\text{-}11) \times 10^{-8}$ dpa/s. Fast reactors could have the same temperature range, but the dose rate is usually ten to hundred times higher [17].

The first step in using the integrated model is finding the total dislocation and single vacancy evolution under the LWR conditions. We use the presented CD model in Section 3 with LWR

irradiation conditions, which we take to be 275 °C and 7 × 10^{-8} dpa/s. The predicted loop size and number density are compared with reported experimental data [17] in Figure 11. The agreement is generally quite good, so we assume the model is performing adequately for qualitative guidance. We need to emphasis that for LWR conditions we use the same E_{b2i} as we used for fast reactors and no refitting is needed.

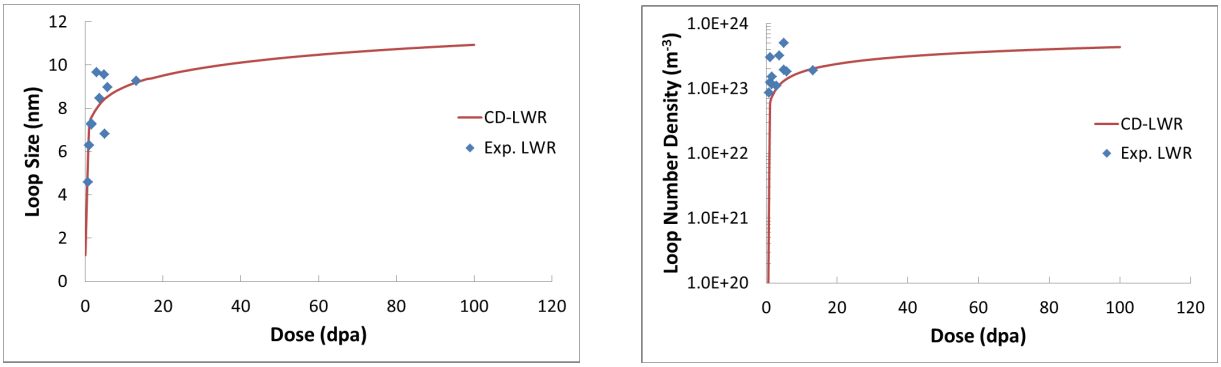

Figure 11. The loop size and loop under density evolution under LWR conditions (275 °C and 7 × 10^{-8} dpa/s) compared with experimental results [17].

After verification of the CD model we use it to predict the evolution of single vacancy and total dislocation properties. Figure 12 shows the evolution of single vacancy and total dislocation density under LWR conditions.

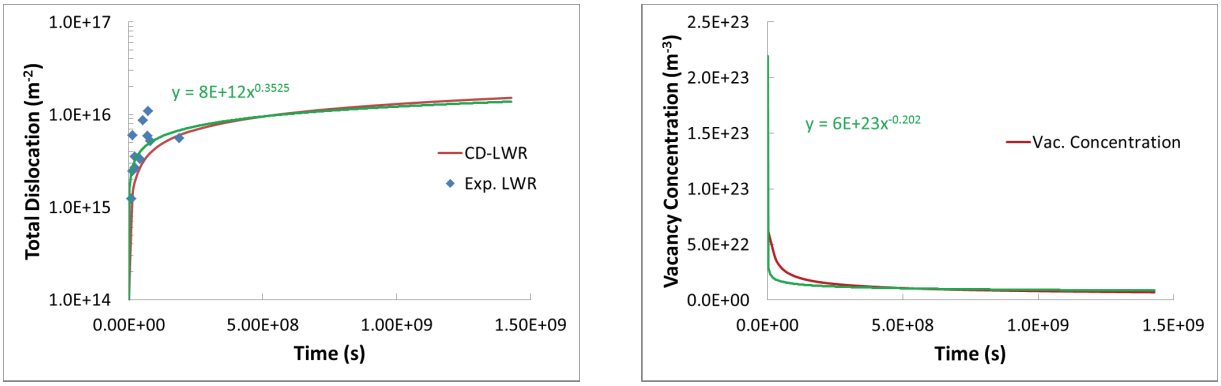

Figure 12. The evolution of total dislocation and single vacancy concentration under LWR irradiation condition (275 °C and 7 × 10^{-8} dpa/s).

The fitted functions for the excess single vacancy and total dislocation density can be used in MatCalc to provide the correct RED and nucleation site numbers in precipitation (discussed in section 4.2).

Figure 13 shows the precipitation of carbide phases ($M_{23}C_6$ and M_6C) under LWR conditions. The first noticeable difference between the carbides precipitation in LWR (Figure 13)

and fast reactors (Figure 6) is the time lag in the transformation of $M_{23}C_6$ to M_6C in LWR conditions. In fast reactors the transformation of $M_{23}C_6$ to M_6C happens from the very beginning of irradiation and M_6C is the dominant phase after 25 dpa (see Figure 6). However, in LWR conditions $M_{23}C_6$ to M_6C transformation starts around 20 dpa and it is much slower than fast reactors such that $M_{23}C_6$ will remain the dominant phase up to 100 dpa. We note that these dpa values are quite approximate as the interfacial energies are obtained by very approximate methods (see Sec. 4.2). Furthermore, the radiation induced dissolution that we hypothesize is occurring for carbides might greatly enhance this transition by enabling facile dissolution and reprecipitation. Overall, understanding that the dpa scale for significant transformation of the carbides may reside within the dpa range of LWR life extension is an important motivation for developing more accurate models.

The other important factor that may cause a big difference in carbide precipitation between LWR and fast reactors is the effect of neutron flux on radiation enhanced dissolution and carbon segregation. As we discussed in Section 4.3 we believe that radiation enhanced dissolution and/or carbon segregation are potentially important factors in precipitation of carbide phases under irradiation. At LWR conditions the dose rate is much lower than fast reactors [17]. Therefore, it is plausible that the radiation enhanced dissolution and/or carbon segregation will be weaker under LWR conditions compared with fast reactor conditions. If that is the case, the volume fraction of carbide would be higher in austenitic stainless steels under LWR conditions compared with fast reactors at the same dose and temperature. The predicted volume fraction from the present model, which does not include radiation enhanced dissolution or carbon segregation, provides an upper bound for the likely volume fraction. We represent the unknown influence of these additional factors by giving a range of LWR values in Figure 13 that includes values starting from those observed in high-flux fast reactor experiments up to those predicted by our model.

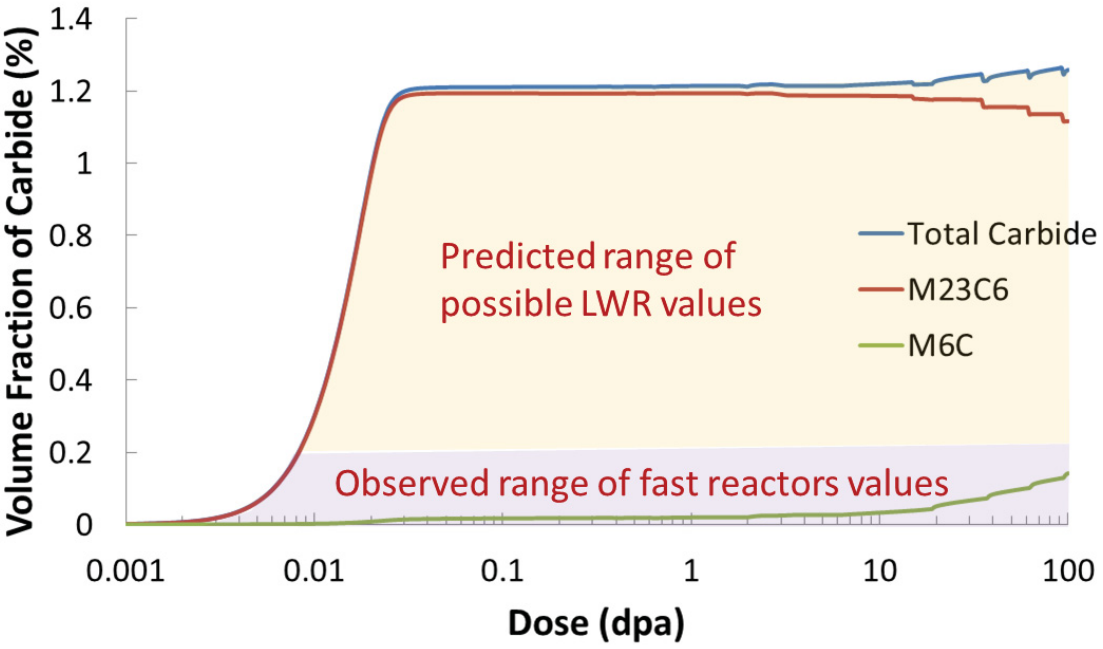

Figure 13. The evolution of total carbide ($M_{23}C_6$ + M_6C) volume fraction under LWR conditions (275 °C and 7 × 10^{-8} dpa/s). The "Predicted range of possible LWR values" covers from those values observed under high flux fast reactor conditions to those predicted from our thermodynamic and kinetic model with no radiation enhanced dissolution, highlighted to represent. We believe the lower neutron flux in LWR conditions can cause higher carbide volume fraction compared with fast reactors due to weaker radiation enhanced dissolution.

Edwards et al. [22] studied experimentally a cold-worked 316 SS baffle bolt which was extracted from the Tihange pressurized water reactor (PWR). In their characterization on the bolt shank, which had been irradiated to 12.2 dpa at 343 °C, they reported the formation of 0.08% volume fraction of γ' (number density of 0.6 × 10^{23} m^{-3} and average size of ~3 nm) and 0.64% volume fraction of an unknown phase (0.2 × 10^{23} m^{-3} and average size of ~8.5 nm). They believed that the identity of the unknown precipitate phase might be some type of carbide. We used our integrated model (CD + OCTANT + MatCalc) to benchmark our prediction against Edwards' result. Edwards did not report the dose rate. Therefore, we use 1 × 10^{-7} dpa/s which is slightly higher than typical LWR dose rate, e.g. 7 × 10^{-8} dpa/s. The CD model reproduces the Edwards' loop size (9.5 nm) and number density (0.85 × 10^{23} m^{-3}) at 12.2 dpa with fitting parameter, $E_{b2i} = 0.6\ eV$ (we do not show the fitting plots). We use the CD predicted vacancy concentration to estimate the RED and then incorporate the RED and dislocation density evolution into MatCalc. We use the Edwards' 316 SS composition as listed in Table 6.

Table 6. Chemical composition (wt.%) for Edwards' 316 SS [22].

Alloy	Fe	Cr	Ni	Mn	Si	C	Mo
316 SS	Bal.	16.7	12.36	1.89	0.72	0.028	2.64

The carbon wt.% in Edwards' alloy in lower than 316 SS that we considered in this work (Table 3). Therefore, we expect to obtain lower carbide volume fraction compared to what we predict for LWR in Figure 13. Figure 14 shows the comparison between the integrated model prediction and the Edwards' volume fraction for carbide phase. The model works very well in predicting the experimental carbide volume fraction. The agreement also supports our hypothesis that the carbide volume fraction under LWR conditions can reach to its thermodynamic asymptotic value, which we do not usually see in fast reactors.

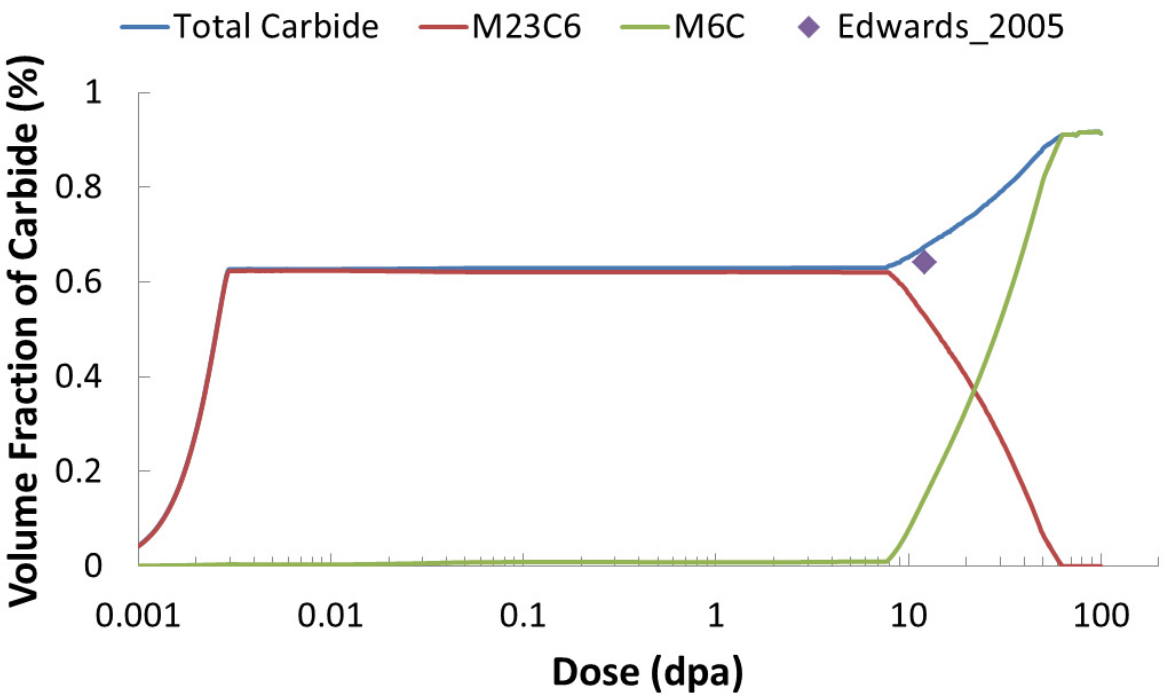

Figure 14. Comparison between integrated model prediction and experimental carbide volume fraction in Edwards' 316 SS [22] under 1×10^{-7} dpa/s irradiation at 343 °C. The good agreement between modeling and experiment supports our hypothesis that the carbide volume fraction under LWR conditions might reach levels significantly higher than typically seen in fast reactors.

For radiation induced phases, i.e. γ' and G-phase, if we assume that the γ' dominancy in cold-worked 316 SS observed at fast reactors is also true for LWR, we can make some predictions about the γ' volume fraction. First, we assume that all γ' form at Frank loops. For γ' precipitation

on Frank loops we use the same "microalloy" methodology we described in Section 4.4. We assume that γ' forms inside a cylindrical RIS region around the loops. Bruemmer et al. [45] reported the evolution of Si segregation at grain boundaries versus neutron irradiation dose up to 9 dpa for LWR conditions. The maximum Si concentration at 9 dpa is 5 wt.%. For Si concentration at higher doses we extrapolate the Si segregation linearly following the Figure 15.

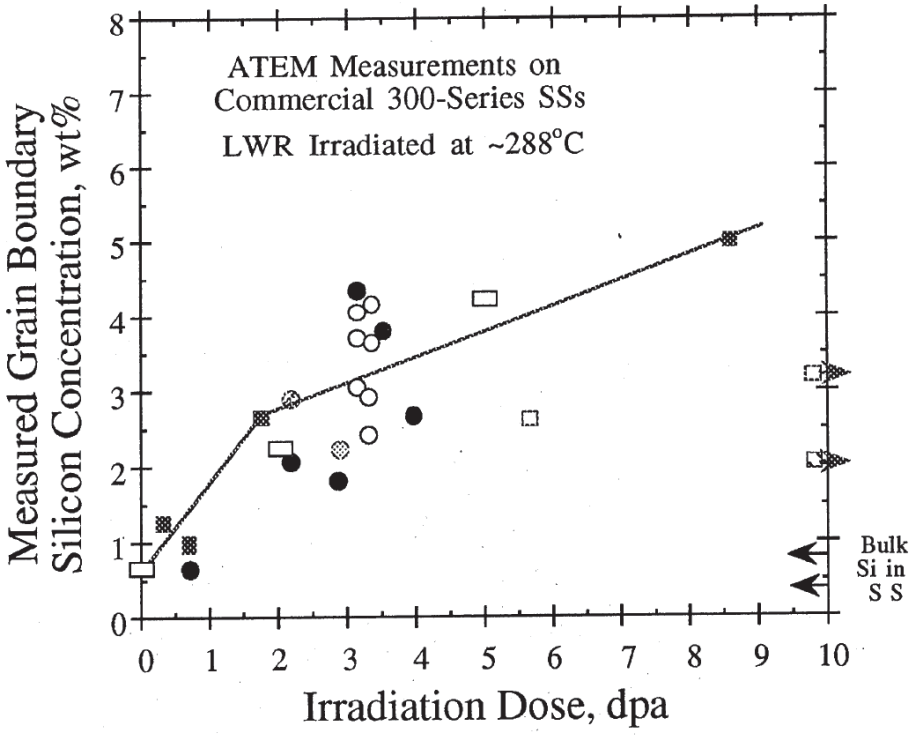

Figure 15. Radiation-induced grain boundary Si concentrations versus neutron irradiation dose for LWR conditions, from [45].

However, the total segregated Si is bounded by the total initial Si content of the alloy. We can find the ultimate possible Si concentration in loops based on the volume fraction of Frank loops and initial concentration of Si in the matrix as follows:

$$W_{Si}^{Aus} = W_{Si}^{RIS} \times V_{RIS}^{Aus}, \tag{25}$$

where W_{Si}^{Aus} is the weight percent of Si in matrix, W_{Si}^{RIS} is the weight percent of Si in RIS region, and V_{RIS}^{Aus} is the volume fraction of RIS region in matrix, which can be calculated by equation 24. For example the linear extrapolation of Figure 15 would give us 9 wt.% Si in the RIS region, but the maximum Si concentration at loops at 20 dpa, with the assumption that all Si in matrix has

segregated to loops, based on equation 25 would be 7.5 wt.%. ($W_{Si}^{Aus} = 0.68\,wt.\%$, initial Si, $V_{RIS}^{Aus} = \pi D_{Loop} \times \pi r_{Cyl}^2 \times N_{Loop} = \pi(9.5\times10^{-9})\times\pi(2\times10^{-9})^2 \times 2.4e23 = 0.09$, D_{Loop} and N_{Loop} come from CD model, Figure 11, and r_{Cyl} is taken from Ref. [38]). If we assume that RIS increases following a linear extrapolation of Figure 15 and that the maximum possible Si in the RIS region consumes the whole Si in matrix then we find the RIS reaches is maximum of 7.5 wt.% at 17 dpa. Within this model no further Si moves to the GB after 17 dpa and, as a result, the γ' volume fraction remains unchanged after 17 dpa.

Using the "microalloy" methodology described in Section 4.4 along with CD results for LWR (Figure 11 and Figure 12) we can predict the evolution of γ' under LWR conditions (Figure 16). For RIS data we use the Si segregation from Figure 15 and for other elements we use the values in Table 5 interpolated up to 17 dpa. We need again to emphasize that the Figure 16 is based on this assumption the segregation to dislocations is similar to experimental segregation data that we have for grain boundaries. While this is clearly an approximate approach, these results suggest that for LWR conditions we might see significantly higher volume fractions of γ' in austenitic steels, approaching 3.5 %, than seen under accelerated fast reactor tests, which were closer to 0.6% (see Figure 10). The difference is primarily due to the lower temperature condition in light water reactors. In particular, at lower temperatures the Frank loops will form more quickly and lead to larger dislocation density, which increased the volume fraction of RIS regions and nucleation sites for forming γ'.

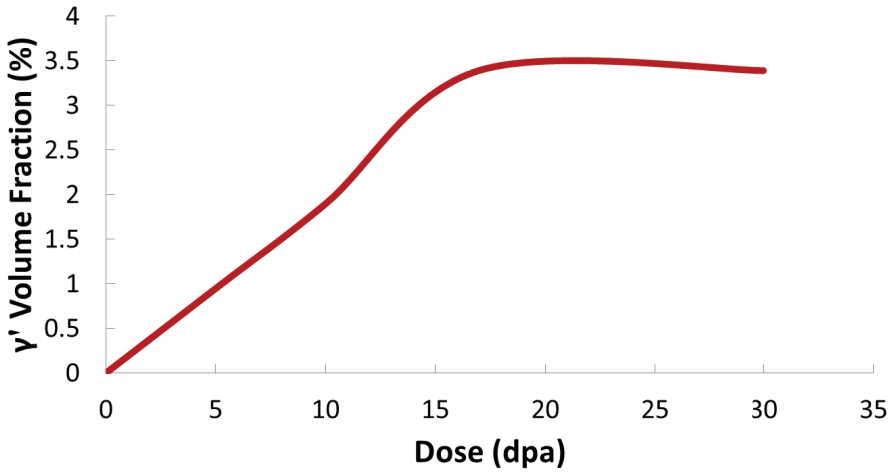

Figure 16. The evolution of volume fraction of γ' under LWR conditions (275 °C and 7 × 10^{-8} dpa/s). The plot is produced based on this assumption that the elements segregation to dislocation is similar to grain boundaries.

The predicted volume fraction for γ' in Figure 16 is quite high and can potentially cause a considerable hardening in base material. A significant sources of uncertainty in our γ' prediction is our simplified RIS model. The volume fraction of γ' in Figure 16 is directly related to Frank loops size and number density, the width of RIS region (i.e. the diameter of RIS tubular region in Figure 7), and the element concentration in the RIS regions. The CD model is fairly successful in predicting the loop behavior (Figure 11) compared with experimental data. The width of RIS region (4 nm) is also based on experimental data [38]. However, the RIS data we used for predicted γ' comes from RIS experimental observations on grain boundaries under LWR conditions, not from measurements on dislocations. As we are not aware of any experimental data on RIS around the dislocations under LWR conditions, we are forced to assume the RIS behavior at dislocations is similar to grain boundaries. One justification for this assumption is the experimental observations of Jiao and Was [37]. They used the the Atom Probe Tomography (APT) technique to study the RIS behavior in 304 SS under 2 MeV proton irradiation to a dose of 5 at 360 °C. They reported that the qualitative RIS behavior (segregation and depletion) of elements at grain boundaries and dislocations were almost identical. More quantitatively, they reported somewhat greater segregation for Fe, Cr, Ni, Mn, and Cu at grain boundaries compared to dislocations. However, for Si it was reverse, and the Si segregation amount was somewhat higher on dislocations than grain boundaries.

We were able to find four papers reporting studies on cold-worked 316 SS under low-flux neutron conditions which could be used for comparison to the prediction in **Figure 16** and we discuss each briefly here.

We are aware of two experimental works on γ' precipitation in cold-worked 316 SS under PWR conditions, Etienne et al. [46] and Edwards et al. [22]. Etienne et al. [46] performed a chemical analyses (used ATP) on a cold-worked 316 SS bolt irradiated up to 12 dpa at 360 °C and Edwards et al. [22] performed a microstructural characterization (used TEM) on a cold-worked 316 SS bolt irradiated up to 12.2 dpa at 343 °C. Neither Etienne nor Edwards reported the dose rate in their experiments, but we will assume they are similar as both bolts were extracted from a PWR. Despite the similarity between materials and irradiation conditions, the results were quite different. Etienne et al. [46] reported a volume fraction of 8.6% for Ni-Si clusters while Edwards reported 0.08% volume fraction for γ'. We believe that the difference may come from different temperatures, different irradiation, and/or different experimental techniques, as the APT has a higher capability to detect small clusters. Etienne reported a ten times higher number density for Ni-Si clusters than Edwards. The Ni-Si clusters number density in Etienne's work similar to the Frank loop number density, which is in agreement with other experimental observation of Ni-Si segregation to Frank loops [37, 38].

Edwards et al. in another work [47] compared the microstructural evolution in stainless steels under LWR and fast reactors conditions (used TEM). They reported no precipitation in two cold-worked 316 SS irradiated at BOR-60 (20 dpa, 9×10^{-7} dpa/s, 320 °C) and in a PWR (33 dpa,

0.5×10^{-7} dpa/s, 290 °C). They also reported very small amount of precipitation (number density $< 10^{21}$ m^{-3} and size ~ 10 nm) in cold-worked 316 SS irradiated in a PWR up to 70 dpa at 315 °C with flux 1×10^{-7} dpa/s. They finally concluded that there are some variations in microstructure over the range of dose rates and total accumulated dose, but these changes are relatively minor.

Finally, Allen et al. [28] studied low flux neutron irradiated (~1×10^{-7} dpa/s) cold-worked 316 SS at 375 °C and did not observe any γ' up to 30 dpa.

This data suggests that a high volume fraction of Ni-Si phase precipitates is at least possible, but also provides a few cases where it has not been observed. Considering the limited available experimental data and the level of variation in the reported data, we believe that the accuracy of our model for predicting γ' precipitation under LWR conditions still needs further study. However, our model does suggest that large γ' precipitate concentrations are possible and that this is an important area for further study.

6 Summary of model assumptions, approximations, and related sources of error

As there are many assumptions and approximations in the overall modeling approach, and the assumptions depend somewhat on what is being simulated, we include here a summary of the major assumptions for convenience. More detailed sensitivity testing on each of these assumptions would be a valuable area for future work.

1. Cluster dynamics (CD) model approximations
   - 1.1. CD model has several input data. Generally, complete set of input data for a complex alloy like 316 SS is not available. We use available parameters in literature and fit the binding energy between dimer interstitials to reproduce data at each flux and temperature. A more accurate model would be able to reproduce data over a range of flux and temperatures and compositions without refitting the parameters.
   - 1.2. Damage efficiency and in-cascade clustering are generally from approximate molecular dynamics and kinetic Monte Carlo simulations of pure iron.
   - 1.3. In CD model of defect we assume that only monomers are mobile. Molecular simulations of some materials, e.g. Ni, have shown that there is a possibility that dimers and trimers be also mobile [48].
   - 1.4. In CD model we assume that the interstitials and vacancies are two dimensional clusters (Frank loop).
   - 1.5. In CD modeling of defect we assume that the sink effects of precipitates for defects are negligible. This assumption is reasonable based on the low precipitate concentration reported in experimental observations [20-22].
   - 1.6. For radiation enhanced diffusion we assume that the elements diffusion is vacancy mediated and the effect of interstitials on elements mobility is negligible.
2. Thermodynamic model (OCTANT) approximations

2.1. OCTANT (thermodynamic database) has some uncertainties for low temperature predictions as no experimental aging data for 316 SS at temperatures lower than 400 °C exist. Similar uncertainties also exist for mobility database.
2.2. Minor elements are not currently available in OCTANT. Some of these elements, e.g. Ti, could have direct effect on alloys precipitation behavior.
2.3. We assume that the irriadiation does not alter the Gibbs free energy of phases.

3. Precipitation model (MatCalc) approximations
3.1. We assume all interfacial energies are given by a simple broken bond model, which may impact significantly what dpa subtle transitions occur (e.g., $M_{23}C_6$ to M_6C). Large errors could also potentially change the qualitative rates for formation of precipitates from the very rapid (<0.1 dpa for a given state of dislocations and RIS) values found in this work.
3.1.1. In precipitation modeling we assume that the RIS matrix composition are constant during a given precipitation evolution to its asymptotic volume fraction. These constant values are reasonable assumption as the kinetics of precipitation at both fast reactor and LWR flux, 9.4×10^{-7} dpa/s and 7×10^{-8} dpa/s, respectively, occurs very quickly (within 0.01 dpa) compared the RIS (several dpa).
3.2. We assume a simple model for stabilization of precipitates on dislocations built into the MatCalc code that may have some significant errors [49].
3.3. In addition to second phase precipitation in austenite matrix, it was shown experimentally that austenite might transform to ferrite after high dose irradiation. This phase transformation could lead to alloy embrittlement [50]. It may also effect on G-phase precipitation as G-phase nucleation at the boundary of austenite and ferrite was observed in duplex steels [51].
3.4. We assume that the carbon mobility is unchanged under irradiation. However, the carbon-vacancy binding may alter the carbon mobility [52].
3.5. Radiation-induced segregation (RIS) model approximations
3.5.1. In quantitative modeling of γ' we assume that the width of RIS "microalloy" region is stationary under irradiation (and it is equal to 4 nm [38]).
3.5.2. The RIS compositions in Table 5 come from different experimental data with different irradiation condition. These data also have high error bar especially for Si, which is the key element in RIP.
3.5.3. We use the grain boundary RIS and assume the same RIS happens to dislocations too.
3.5.4. For high doses where RIS data is not available, we use linear extrapolation of available data. We assume that this extrapolated RIS is bounded by the value at which all Si is in the RIS "microalloy" region.

4. In γ' precipitation we only consider the RIS on dislocations. This is a reasonable assumption because the dislocations are preferable nucleation sites for γ' [41] and also because the concentration of other sinks, e.g. grain boundaries, is much less than dislocations.

7 Conclusion

A thermo-kinetic model was developed to study the second phase precipitation in 300 series austenitic stainless steels, with a focus on cold-worked 316 stainless steels. We compare to data for a fast reactor flux of 9.4×10^{-7} dpa/s and temperatures of 390 °C and predict behavior for LWR conditions of 7×10^{-8} dpa/s and 275 °C. The composition used for all models is given in Table 1 and Table 5 (except for Figure 14, which uses the composition in **Table 6**). The approach integrated a cluster dynamics model for radiation enhanced diffusion and dislocation nucleation site parameters, the OCTANT database for thermodynamics, and MatCalc for kinetic parameters and solving the precipitation model. The main results of this work are as follows.

1. Fast reactor test conditions (9.4×10^{-7} dpa/s, 390 °C)
   1.1. The model was successful in semi-quantitative prediction of volume fraction of γ' phase and showed discrepancy with carbides that likely due to the absence of radiation induced dissolution physics in the model.
   1.2. The results supported the fact that γ' is the dominant phase in "microalloy" regions of enriched solutes occurring due to RIS at dislocation loops. The OCTANT also predicted some G-phase, but as we do not see G-phase in the experimental observations of irradiated cold-worked 316 SS, maybe due to overestimated interfacial energy, we suspend G-phase in our calculations.
   1.3. We showed that in the formation of γ' it is the time scale of radiation induced segregation (i.e., the formation of the "microalloy" region) that controls the γ' formation, not the kinetics of γ' precipitation from the matrix, which takes place over less than ~0.01 dpa once the RIS is established.
   1.4. Carbides form 1.2% volume fraction $M_{23}C_6$ within 0.1 dpa, which gets replaced gradually by M_6C while increasing to a final volume fraction of 1.7% at about 23 dpa. These results are fully consistent with high-temperature experimental ageing data. However, the saturation volume fraction in modeling is about one order of magnitude higher than most irradiation experimental data. We propose the radiation enhanced dissolution and/or carbon depletion at sinks as the sources of this discrepancy. Under the radiation enhanced dissolution hypothesis, competition between radiation enhanced precipitation and dissolution provides a non-equilibrium steady state situation for carbides which is far from thermal equilibrium and yields a quite low volume fraction around 0.1-0.2%. Carbon depletion at dislocations and grain boundaries also may lead to reduced carbide nucleation and growth at sinks and potentially homogeneous carbide nucleation, giving smaller carbide particles that are difficult to observe experimentally.

1.5. Carbide behavior reaches steady state at about 23 dpa, which suggests that higher doses are unlikely to alter their volume fraction. However, as they are governed by a balance between driving forces for precipitation and dissolution, small changes in flux, temperature, or composition could alter their volume fraction significantly. The γ' phase forms from RIS on dislocations in about 0.01 dpa, but RIS takes several dpa to form on an existing dislocation.

2. LWR conditions (7×10^{-8} dpa/s, 275 °C)
   2.1. The model predicted that $M_{23}C_6$ would saturate at the very beginning of irradiation. However, the transformation of $M_{23}C_6$ to M_6C was slower in LWR compared with fast reactors and $M_{23}C_6$ remained the dominant carbide phase up to 100 dpa.
   2.2. In LWR the Frank loops are smaller and more numerous (because of low temperature condition i.e. 275 °C) compared with fast reactors. If we assume similar RIS for dislocation as measure for grain boundaries (Figure 15), we can predict that all Si in 316 SS matrix will segregate to dislocations within 17 dpa.
   2.3. The integrated model along with experimental RIS predicted the maximum volume fraction of γ' to be ~3.5% under LWR conditions.
   2.4. We believe that radiation enhanced dissolution is an important factor in carbide precipitation. Under LWR conditions the radiation enhanced dissolution is expected to be weaker than fast reactors, which could lead to formation of significantly more carbides in LWR vs. fast reactor conditions. Based on our thermodynamic models this increase in carbide volume fraction could be up to about 1.2%, or an approximately ten-fold increase.

This work has led to a useful model that can be readily adapted to new temperature, flux, and fluence conditions in austenitic stainless steels. Through our focus on cold-worked 316 SS we have developed a new understanding of the time scales and mechanisms governing the formation and evolution under irradiation of the key precipitate phases: carbides, γ', and G-phase.

8 Areas for possible future work

1. Models and experiments are needed to study the RIS on dislocations at LWR conditions. If the RIS on dislocations follows the same trend as we see in grain boundaries, the γ' could have a noticeable effect on austenitic steels embrittlement under LWR extended life.

2. Experimental data on microstructural evolution in austenitic steels under LWR flux and temperature is needed for modeling refinement and validation.

3. Interfacial energies play crucial roles on kinetics of precipitates. A set of experimental or molecular simulation studies could greatly improve the reliability of the model interfacial energies.

4. Current thermodynamic databases need to be more rigorous for low temperatures (~300 °C). One possible option is DFT-based Calphad models.
5. The impact of radiation enhanced dissolution and carbon segregation could change our perspective on carbide evolution in fast reactor data and their possible extension to LWR conditions. Numerical modeling and experiment are needed to understand the potency of these phenomena and their flux and temperature dependence.
6. A more rigorous Cluster Dynamics model which includes more mobile species and He effects would be beneficial.
7. A model for radiation enhanced dissolution needs to be developed for the carbides and perhaps also other phases.
8. An integrated model that extends MatCalc to rigorously include the radiation effects (e.g., radiation enhanced diffusion, radiation enhanced dissolution, and loop and void formation) needs to be developed.

References

1. Laborne, A.R., et al., *Correlation of radiation-induced changes in microstructure/microchemistry, density and thermo-electric power of type 304L and 316 stainless steels irradiated in the Phénix reactor.* Journal of Nuclear Materials, 2015. **460**: p. 72-81.
2. Yang, Y. and J. Busby, *Thermodynamic modeling and kinetics simulation of precipitate phases in AISI 316 stainless steels.* Journal of Nuclear Materials, 2014. **448**(1): p. 282-293.
3. Kozeschnik, E. and B. Buchmayr. *MATCALC- a simulation tool for multicomponent thermodynamics, diffusion and phase transformations*. in *Fifth International Seminar on the Numerical Analysis of Weldability*. 1999.
4. Shim, J.-H., et al., *Modeling precipitation thermodynamics and kinetics in type 316 austenitic stainless steels with varying composition as an initial step toward predicting phase stability during irradiation.* Journal of Nuclear Materials, 2015. **462**: p. 250-257.
5. Cohen, S.D. and A.C. Hindmarsh, *CVODE, a stiff/nonstiff ODE solver in C.* Computers in physics, 1996. **10**(2): p. 138-143.
6. Christien, F. and A. Barbu, *Effect of self-interstitial diffusion anisotropy in electron-irradiated zirconium: A cluster dynamics modeling.* Journal of nuclear materials, 2005. **346**(2): p. 272-281.
7. Duparc, A.H., et al., *Microstructure modelling of ferritic alloys under high flux 1 MeV electron irradiations.* Journal of nuclear materials, 2002. **302**(2): p. 143-155.
8. Gokhman, A. and F. Bergner, *Cluster dynamics simulation of point defect clusters in neutron irradiated pure iron.* Radiation Effects & Defects in Solids: Incorporating Plasma Science & Plasma Technology, 2010. **165**(3): p. 216-226.
9. Pokor, C., et al., *Irradiation damage in 304 and 316 stainless steels: experimental investigation and modeling. Part I: Evolution of the microstructure.* Journal of Nuclear Materials, 2004. **326**(1): p. 19-29.
10. Ribis, J., et al., *Experimental study and numerical modelling of the irradiation damage recovery in zirconium alloys.* Journal of Nuclear Materials, 2010. **403**(1): p. 135-146.
11. Phythian, W., et al., *A comparison of displacement cascades in copper and iron by molecular dynamics and its application to microstructural evolution.* Journal of nuclear materials, 1995. **223**(3): p. 245-261.
12. Osetsky, Y.N., et al., *Vacancy loops and stacking-fault tetrahedra in copper: I. Structure and properties studied by pair and many-body potentials.* Philosophical Magazine A, 1999. **79**(9): p. 2259-2283.

13. Soneda, N. and T.D. De La Rubia, *Defect production, annealing kinetics and damage evolution in α-Fe: an atomic-scale computer simulation.* Philosophical Magazine A, 1998. **78**(5): p. 995-1019.

14. Ghoniem, N. and D. Cho, *The simultaneous clustering of point defects during irradiation.* physica status solidi (a), 1979. **54**(1): p. 171-178.

15. Barashev, A., S. Golubov, and R. Stoller, *A Model of Radiation-induced Microstructural Evolution.* ORNLLTR-2014487, 2014.

16. Stoller, R.E. and G.R. Odette. *A composite model of microstructural evolution in austenitic stainless steel under fast neutron irradiation*. in *Radiation-Induced Changes in Microstructure, 13th International Symposium, ASTM STP*. 1987.

17. Gan, J., G. Was, and R. Stoller, *Modeling of microstructure evolution in austenitic stainless steels irradiated under light water reactor condition.* Journal of nuclear materials, 2001. **299**(1): p. 53-67.

18. Ehrhart, P., et al., *Atomic Defects in Metals*. Vol. 25. 1991: Springer.

19. Odette, G., T. Yamamoto, and D. Klingensmith, *On the effect of dose rate on irradiation hardening of RPV steels.* Philosophical Magazine, 2005. **85**(4-7): p. 779-797.

20. Tan, L., K.G. Field, and J.T. Busby, *Analysis of Phase Transformation Studies in Solute Addition Alloys.* ORNLTM-2014303, 2014.

21. Edwards, D., A. Schemer-Kohrn, and S. Bruemmer, *Characterization of neutron-irradiated 300-series stainless steels.* EPRI, Palo Alto, CA, 2006. **1009896**.

22. Edwards, D.J., et al., *Influence of irradiation temperature and dose gradients on the microstructural evolution in neutron-irradiated 316SS.* Journal of nuclear materials, 2003. **317**(1): p. 32-45.

23. Yang, Y., L. Tan, and J.T. Busby, *Thermal Stability of Intermetallic Phases in Fe-rich Fe-Cr-Ni-Mo Alloys.* Metallurgical and Materials Transactions A, 2015. **46**(9): p. 3900-3908.

24. Tan, L. and Y. Yang, *In situ phase transformation of Laves phase from Chi-phase in Mo-containing Fe–Cr–Ni alloys.* Materials Letters, 2015. **158**: p. 233-236.

25. Renault-Laborne, A., et al., *Characterization of Precipitates in 316 Stainless Steel Neutron-Irradiated at 390 C by the Combination of CDF-TEM, EF-TEM, and HR-TEM.* 2014.

26. Renault, A.-É., et al. *Microstructure and grain boundary chemistry evolution in austenitic stainless steels irradiated in the BOR-60 reactor up to 120 dpa, 14th Int*. in *Conf. on Environmental Degradation of Materials in Nuclear Power Systems, Virginia Beach, VA*. 2009.

27. Hashimoto, N., et al., *Microstructure of austenitic stainless steels irradiated at 400 C in the ORR and the HFIR spectral tailoring experiment.* Journal of nuclear materials, 2000. **280**(2): p. 186-195.

28. Allen, T.R., et al., *Properties of 20% Cold-Worked 316 Stainless Steel Irradiated at Low Dose Rate.* Effects of Radiation on Materials, ASTM STP, 2004. **1447**.

29. Svoboda, J., et al., *Modelling of kinetics in multi-component multi-phase systems with spherical precipitates: I: Theory.* Materials Science and Engineering: A, 2004. **385**(1): p. 166-174.

30. Sonderegger, B. and E. Kozeschnik, *Generalized nearest-neighbor broken-bond analysis of randomly oriented coherent interfaces in multicomponent fcc and bcc structures.* Metallurgical and Materials Transactions A, 2009. **40**(3): p. 499-510.

31. Maziasz, P., *The formation diamond-cubic eta (η) phase in type 316 stainless steel exposed to thermal aging or irradiation environments.* Scripta Metallurgica, 1979. **13**(7): p. 621-626.

32. Maziasz, P., *Overview of microstructural evolution in neutron-irradiated austenitic stainless steels.* Journal of nuclear materials, 1993. **205**: p. 118-145.

33. Weiss, B. and R. Stickler, *Phase instabilities during high temperature exposure of 316 austenitic stainless steel.* Metallurgical Transactions, 1972. **3**(4): p. 851-866.

34. Lai, J., *A study of precipitation in AISI type 316 stainless steel.* Materials Science and Engineering, 1983. **58**(2): p. 195-209.

35. National Institute for Materials Science (NIMS). *Diffusion Database*. [cited 2015; Available from: http://diffusion.nims.go.jp/index_en.html.

36. Goldschmid, H.J., *Interstitial alloys*. 2013: Springer.

37. Jiao, Z. and G. Was, *Novel features of radiation-induced segregation and radiation-induced precipitation in austenitic stainless steels.* Acta Materialia, 2011. **59**(3): p. 1220-1238.

38. Hatakeyama, M., S. Tamura, and I. Yamagata, *Direct observation of solute–dislocation interaction on screw dislocation in a neutron irradiated modified 316 stainless steel.* Materials Letters, 2014. **122**: p. 301-305.

39. Russell, K.C., *Phase stability under irradiation.* Progress in Materials Science, 1984. **28**(3): p. 229-434.

40. Nelson, R., J. Hudson, and D. Mazey, *The stability of precipitates in an irradiation environment.* Journal of Nuclear Materials, 1972. **44**(3): p. 318-330.

41. Lee, E., P. Maziasz, and A. Rowcliffe, *Structure and composition of phases occurring in austenitic stainless steels in thermal and irradiation environments*. 1980, Oak Ridge National Lab., TN (USA).

42. Lee, E. and L. Mansur, *Relationships between phase stability and void swelling in Fe-Cr-Ni alloys during irradiation.* Metallurgical Transactions A, 1992. **23**(7): p. 1977-1986.

43. Cawthorne, C. and C. Brown, *The occurrence of an ordered FCC phase in neutron irradiated M316 stainless steel.* Journal of Nuclear Materials, 1977. **66**(1): p. 201-202.

44. Maziasz, P. and C. McHargue, *Microstructural evolution in annealed austenitic steels during neutron irradiation.* International materials reviews, 1987. **32**(1): p. 190-219.

45. Bruemmer, S.M., et al., *Radiation-induced material changes and susceptibility to intergranular failure of light-water-reactor core internals.* Journal of Nuclear Materials, 1999. **274**(3): p. 299-314.

46. Etienne, A., et al., *Tomographic atom probe characterization of the microstructure of a cold worked 316 austenitic stainless steel after neutron irradiation.* Journal of Nuclear Materials, 2008. **382**(1): p. 64-69.

47. Edwards, D., et al., *MICROSTRUCTURAL EVOLUTION IN NEUTRON-IRRADIATED STAINLESS STEELS: COMPARISON OF LWR AND FAST-REACTOR IRRADIATIONS*, in *TMS (The Minerals, Metals & Materials Society)*, T.R. Allen, P.J. King, and L. Nelson, Editors. 2005. p. 419-428.

48. Lam, N. and L. Dagens, *Calculations of the properties of single and multiple defects in nickel.* Journal of Physics F: Metal Physics, 1986. **16**(10): p. 1373.

49. Radis, R. and E. Kozeschnik, *Numerical simulation of NbC precipitation in microalloyed steel.* Modelling and Simulation in Materials Science and Engineering, 2012. **20**(5): p. 055010.

50. Margolin, B., et al., *Prediction of the effects of thermal ageing on the embrittlement of reactor pressure vessel steels.* Journal of Nuclear Materials, 2014. **447**(1): p. 107-114.

51. Hamaoka, T., et al., *Accurate determination of the number density of G-phase precipitates in thermally aged duplex stainless steel.* Philosophical Magazine, 2012. **92**(22): p. 2716-2732.

52. Slane, J., C. Wolverton, and R. Gibala, *Experimental and theoretical evidence for carbon-vacancy binding in austenite.* Metallurgical and Materials Transactions A, 2004. **35**(8): p. 2239-2245.

53. Renault, A., et al., *TEM and EFTEM characterization of solution annealed 304L stainless steel irradiated in PHENIX, up to 36 dpa and at 390 °C.* Journal of Nuclear Materials, 2012. **421**: p. 124-131.

9 Appendix A: Mole fraction to volume fraction conversion

MatCalc and other precipitation modeling tools usually calculate the amount of the second phase precipitates as mole fraction. However, experimental data generally express the amount of precipitates as volume fraction. To be consistent, we need to convert the MatCalc output to volume fraction. The volume fraction of a phase *X* in austenite matrix can be calculated from its mole fraction as following,

$$Volume\ fraction\ of\ X = mole\ fraction\ of\ X \times \frac{V_X^m}{V_{Austenite}^m}\ , \qquad \text{(A1)}$$

where V_X^m is the molar volume of the phase *X*. Molar volume of a solid phase is;

$$V_m = \frac{V_{cell} N_A}{N}, \qquad \text{(A2)}$$

where V_{cell} is volume of crystallographic cell, N_A Avogadro number, and N total number of atoms per unit cell. Table A1 shows the crystal structure, lattice size, and number of atoms per lattice site for 316 SS, $M_{23}C_6$, M_6C, and γ'.

Table A1. Precipitate phases found in austenitic stainless steels

Phase	Crystal type	Lattice parameter	Number of atoms per lattice site
Austenite (316 SS)	FCC	3.6 Å	4
$M_{23}C_6$	FCC	10.6 Å	92
M_6C	FCC	10.8 Å	96
γ' (Ni_3Si)	FCC	3.5 Å	4

Using the data in Table A1 we can calculate the molar volume of each phase.

$$V_{m,Austenite} = \frac{V_{cell} N_A}{N} = \frac{(3.6e-10)^3 \times 6.02e23}{4} = 7.0e-6$$

$$V_{m,M23C6} = \frac{V_{cell} N_A}{N} = \frac{(10.6e-10)^3 \times 6.02e23}{92} = 7.8e-6$$

$$V_{m,M6C} = \frac{V_{cell} N_A}{N} = \frac{(10.8e-10)^3 \times 6.02e23}{96} = 7.8e-6$$

$$V_{m,\gamma'} = \frac{V_{cell} N_A}{N} = \frac{(3.5e-10)^3 \times 6.02e23}{4} = 6.4e-6$$

And finally the relation between volume fraction and mole fraction of each phase would be:

$$V_{f\_M23C6} = 1.1 M_{f\_M23C6} \quad \text{(A3)}$$

$$V_{f\_M6C} = 1.1 M_{f\_M6C} \quad \text{(A4)}$$

$$V_{f\_\gamma'} = 0.9 M_{f\_\gamma'} \quad \text{(A5)}$$

10 Appendix B: Experimental data on precipitation volume fraction in 300 series austenitic stainless steels under neutron irradiation.

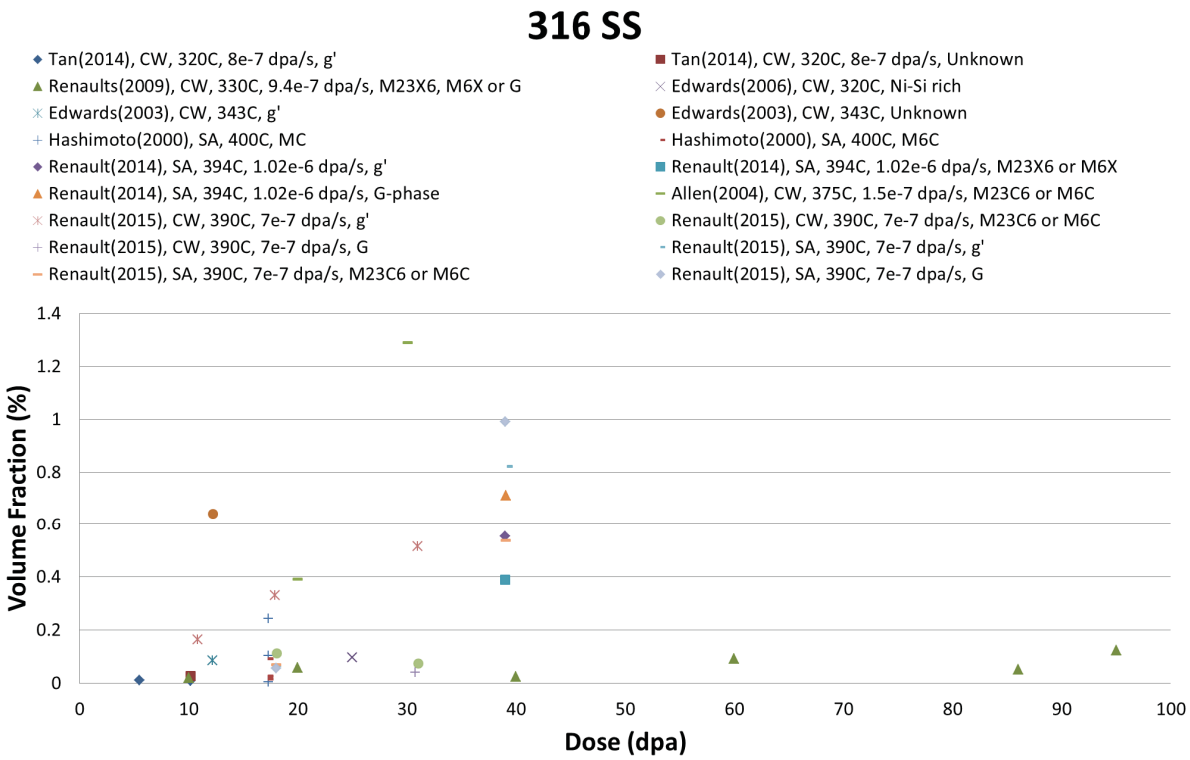

Figure 17. Experimental data on volume fraction of different phases in 316 SS under neutron irradiation at temperatures between 300 °C to 400 °C.

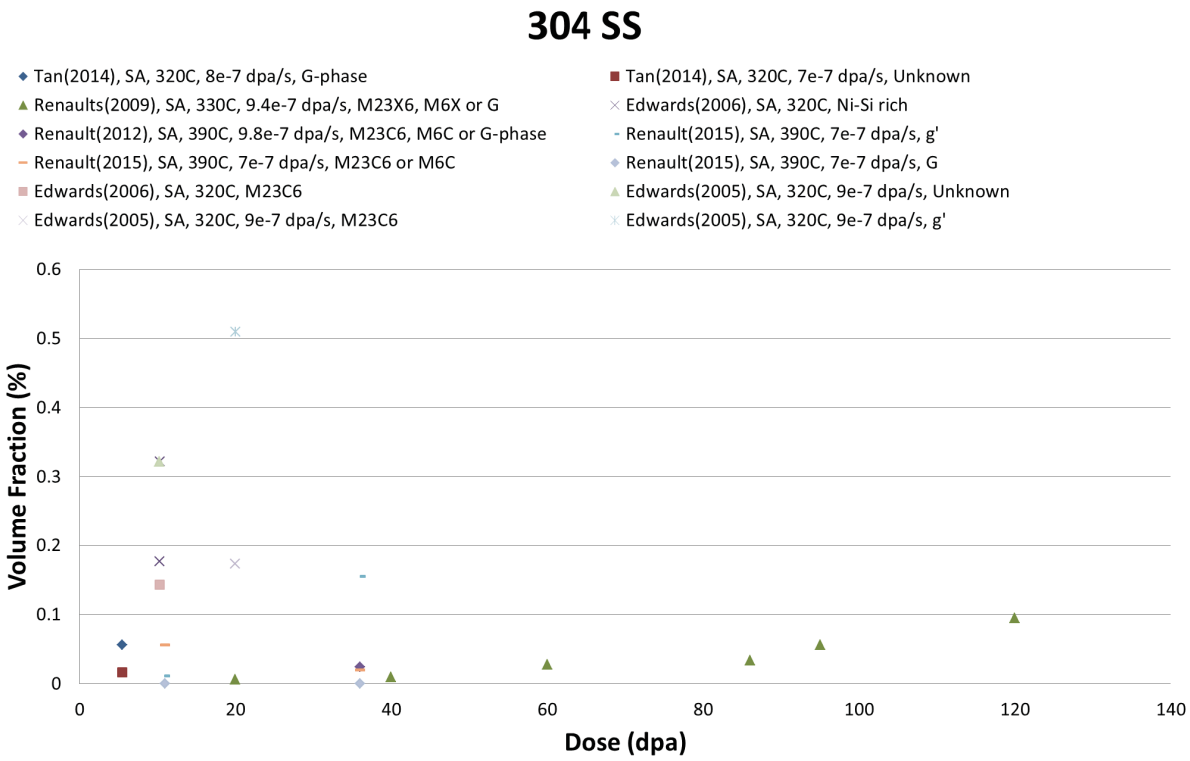

Figure 18. Experimental data on volume fraction of different phases in 304 SS under neutron irradiation at temperatures between 300 °C to 400 °C.

Allen (2004) [28]

Edwards (2003) [22]

Edwards (2005) [47]

Edwards (2006) [21]

Hashimoto (2000) [27]

Renault (2012) [53]

Renault (2009) [26]

Renault (2014) [25]

Renault (2015) [1]

Tan (2014) [20]